University of Illinois at Urbana-Champaign

ACRC

Air Conditioning and Refrigeration Center A National Science Foundation/University Cooperative Research Center

Condensation of CO_2 at Low Temperature inside Horizontal Microfinned Tubes

J. Zilly, J. Jang, and P. S. Hrnjak

ACRC CR-49 March 2003

For additional information:

Air Conditioning and Refrigeration Center
University of Illinois
Mechanical & Industrial Engineering Dept.
1206 West Green Street
Urbana, IL 61801

(217) 333-3115

Prepared for
Wolverine Tube Inc.

The Air Conditioning and Refrigeration Center was founded in 1988 with a grant from the estate of Richard W. Kritzer, the founder of Peerless of America Inc. A State of Illinois Technology Challenge Grant helped build the laboratory facilities. The ACRC receives continuing support from the Richard W. Kritzer Endowment and the National Science Foundation. The following organizations have also become sponsors of the Center.

Alcan Aluminum Corporation
Amana Refrigeration, Inc.
Arçelik A. S.
Brazeway, Inc.
Carrier Corporation
Copeland Corporation
Dacor
Daikin Industries, Ltd.
Delphi Harrison Thermal Systems
Embraco S. A.
General Motors Corporation
Hill PHOENIX
Honeywell, Inc.
Hydro Aluminum Adrian, Inc.
Ingersoll-Rand Company
Kelon Electrical Holdings Co., Ltd.
Lennox International, Inc.
LG Electronics, Inc.
Modine Manufacturing Co.
Parker Hannifin Corporation
Peerless of America, Inc.
Samsung Electronics Co., Ltd.
Sanyo Electric Co., Ltd.
Tecumseh Products Company
The Trane Company
Valeo, Inc.
Visteon Automotive Systems
Wieland-Werke, AG
Wolverine Tube, Inc.

For additional information:

Air Conditioning & Refrigeration Center
Mechanical & Industrial Engineering Dept.
University of Illinois
1206 West Green Street
Urbana, IL 61801

217 333 3115

Summary

Enhanced tubes have been commonly used in heat exchangers for 30 years. Modern micro-fin tubes play a significant role in high-efficiency refrigerators and air conditioners with their significantly enhanced heat transfer coefficients and low pressure loss characteristics. Experimental data for condensation exist for commonly used refrigerants but not for CO_2 at low temperatures. This study investigates inner heat transfer coefficient and pressure drop during condensation of CO_2 inside micro-fin tubes at low temperatures.

A test rig has been build to measure heat transfer coefficients in horizontal condenser pipes and adiabatic horizontal and vertical pressure drop at low temperatures. Heat transfer coefficients and pressure drop are measured at different mass flux, qualities, saturation and wall temperatures. Correlations for commonly used refrigerants and higher condensation temperatures are used to predict measured data for CO_2 at low temperatures. Results for micro-fin tubes with new geometric parameters are compared to smooth tube data.

Main results are the fact that the heat transfer coefficients of the investigated micro-fin tube are less dependent on mass flux as heat transfer coefficients of smooth tubes. It was found that lower saturation temperature results in higher heat transfer coefficients and pressure drop for the micro-fin tube similar to the smooth tube. Heat transfer coefficients for micro-fin tubes are not dependent on the temperature difference between saturation temperature and inner wall temperature. The experimental data for both the smooth and the micro-fin tube were over predicted by correlations. Enhancement factors show that micro-fin tubes increase heat transfer coefficients most for low mass flux and high qualities. At that conditions heat transfer coefficients for the micro-fin tube are 3 times higher than for the smooth tube. Penalty factors indicate that the increase in pressure drop is highest for low mass flux and low qualities. At that conditions penalty factors are 1.9 decreasing to 1.2 for high qualities. Further research will be done on other geometrical parameters including different tube diameters for micro-fun tubes.

Table of Contents

List of Figures

Page

List of Tables

Page

Notation and Definitions

Symbol	Description	Unit
A	Area	m^2
Af	Fin Area	m^2
c_p	Isobaric thermal capacity	$kJ \cdot kg^{-1} \cdot K^{-1}$
D	Diameter	mm
e	Roughness	m
f	Friction factor	-
g	Gravitational constant	$m \cdot s^{-2}$
G	Mass flux	$kg \cdot m^{-2} \cdot s^{-1}$
gf	Fin gap	mm
h	Enthalpy	$kJ \cdot kg^{-1}$
hf	Fin height	mm
L	Length	m
$\dot{m}$	Mass flow	$kg \cdot s^{-1}$
n	Element variable	-
nf	Fin number	-
p	Pressure	kPa
P	Perimeter	m
pf	Fin perimeter	m
$\dot{Q}$	Heat flow	W
Rx	Geometry enhancement factor	-
s	Wall thickness	-
t	Temperature	°C
u	Fluid velocity	$m \cdot s^{-1}$
UA	Heat transfer coefficient times surface area	$W \cdot K^{-1}$
x	Quality, vapor fraction	-
z	Coordinate in flow direction	-

Greek	Description	Unit
α	Heat Transfer Coefficient	$W \cdot m^{-2} \cdot K^{-1}$
β	Spiral or helix angle	°
δ	Uncertainty	-
Δ	Difference	-
ε	Void fraction	-
ϕ	Inclination angle	°
γ	Apex angle	°
η	Area enlargement factor	-
φ	Heat flow of finite elements	W
λ	Thermal conductivity	$W \cdot m^{-1} \cdot K^{-1}$
μ	Dynamic viscosity	$kg \cdot m^{-1} \cdot s^{-1}$
ν	Kinematic viscosity	$mm^2 \cdot s^{-1}$
?	Density	$kg \cdot m^{-3}$
σ	Surface tension	$N \cdot m^{-1}$

Superscripts	Description	Unit
'	Saturated liquid	
"	Saturated vapor	
amb	Ambient, environmental	
c	Corrected	
cal	Calorimeter	
calc	Calculated	
crit	Critical	
cs	Cross sectional	

Subscripts	Description	Unit
b	Natural convective	
c	Correction	
eff	Effective	
el	Electric	
elt	Element	
eq	Equivalent	
F	Forced	
f	Frictional	
ff	Free flow	
ft	Fin top	
g	Gravitational	
h	Hydraulic	
ho	Horizontal	
i	Inner	
in	At inlet	
l	Liquid	
lo	Assuming whole refrigerant is liquid	
loss	Loss	
lv	Vaporization, liquid vapor	
m	Mean	
max	Maximum	
melt	Meltdown	
min	Minimum	
o	Outer	
out	At outlet	
P	Pump	
red	Reduced	
ref	Reference	
sat	Saturated	
ts	At test section	
v	Vapor	
ve	Vertical	
vo	Assuming whole refrigerant is vapor	
w	Wall	

Abbreviations	Description	Unit
CFC	Chlorofluorocarbon	
COP	Coefficient of performance	
Cu	Copper	
EF	Enhancement Factor	
EES	Engineering Equation solver	
HCFC	Hydrochlorofluorocarbon	
HFE	Cooling fluid	
HTC	Heat Transfer Coefficient	$W \cdot m^{-2} \cdot K^{-1}$
LMTD	Logarithmic Mean Temperature Difference	K
Sn	Tin	
PF	Penalty factor	

Table 1: List of Dimensionless Numbers

Group	Interpretation	Definition	Range
Bond number	Ratio of gravitational to surface tension forces	$Bb = \frac{(\rho_l - \rho_v) \cdot g \cdot D^2}{\sigma}$	19 - 76
Froude number	Ratio of inertial to gravitational forces	$Fr = \frac{V_l}{\sqrt{g \cdot D}} = \frac{G/\rho_l}{\sqrt{g \cdot D}}$ $Fr^2 = \frac{V_l^2}{g \cdot D} = \frac{(G/\rho_l)^2}{g \cdot D}$	0.08 - 4.56 0.007 - 20.8
Galileo number	Ratio of gravitational to viscous forces	$Ga = \frac{\rho_l \cdot (\rho_l - \rho_v) \cdot g \cdot D^3}{\mu_l^2}$	$1.05 \cdot 10^{-7}$ - $1.76 \cdot 10^{-8}$
Jakob number	Ratio of sensible to latent energy transfer	$Ja = \frac{c_{pl} \cdot (t_{sat} - t_w)}{i_{lv}}$	0.01 - 0.06
Nusselt number	Dimensionless heat transfer number	$Nu = \frac{h \cdot D}{k_l}$	50 - 1000
Prandtl number	Ratio of momentum diffusivity to heat diffusivity	$Pr = \frac{\mu \cdot c_p}{k_l}$	2.1 - 3.8 for liquid 0.8 - 1.5 for vapor
Weber number	Ratio of internal to surface tension forces	$We = \frac{G^2 \cdot D}{\rho_v \cdot \sigma}$	6 - 10000
Reynolds number	Ratio of internal to viscous forces	$Re = \frac{G \cdot D}{\mu}$	listed below
Superficial Reynolds number	Assumes that actual phase flow rate occupies entire tube	$Re_l = \frac{G(1-x) \cdot D}{m_l}$ $Re_v = \frac{G(1-x) \cdot D}{m_v}$	50 - 26000 600 - 351000

Group	Interpretation	Definition	Range
Liquid or vapor only Reynolds number	Assumes all flow consists of the phase of interest and occupies entire tube	$\mathrm{Re}_{lo} = \frac{G \cdot D}{m_{lo}}$ $\mathrm{Re}_{vo} = \frac{G \cdot D}{m_{vo}}$	900 - 27000 12000 - 370000
Lockhart-Martinelli parameter	Liquid inventory	$X_{tt} = \left(\frac{r_v}{r_l}\right)^{0.5} \cdot \left(\frac{m_l}{m_v}\right)^{0.1} \cdot \left(\frac{1-x}{x}\right)^{0.9}$	0.018 - 6

1. Introduction

CO_2 was widely used as a refrigerant before the Second World War but the introduction of CFC and HCFC refrigerants led to a discontinuation of its use. These new refrigerants were developed by the chemical industry to be stable in refrigerant systems for their lifetime. This characteristic feature turned out to be harmful for earth's atmosphere as the refrigerant once released into the environment does not disintegrate. It was assumed that the chemically inert CHF and HCFC molecules would not react in the atmosphere at all, but in 1974 a publication by Rowland and Molina [01] described a complicated catalytic reaction of chlorofluorocarbons that could deplete earth's ozone layer. In addition it was found by using spectral analysis that the spectrum of each CFC and HCFC compound is unique in the atmosphere and that these compounds therefore absorb frequencies out of the sunlight that have not influenced earth's energy balance before.

In the search for environmentally save technology, the natural refrigerant CO_2 receives more interest again. CO_2 is a non-toxic and non-flammable fluid, it has no Ozone Depletion Potential and no Global Warming Potential. Chemical stability of CO_2 is high as it has a very low energy level compared to other carbon compounds. Higher pressures, lower thermodynamic efficiency and lower heat transfer coefficients on the other hand are disadvantageous characteristics of CO_2. But with today's technology it is possible to handle high pressure systems and the heat transfer coefficients can be increased significantly by adjusting heat exchangers to the physical properties of CO_2.

Many different ways to improve a heat exchanger exist. They may use passive techniques as rough surface, extended surface, displaced insert, coiled tubes or active techniques as surface vibration, fluid vibration and electrostatic fields. Work on internally finned tubes was slow to develop, because practical manufacturing techniques to form internal fins did not exist until the late 1960s. Many models have been developed for condensation of refrigerants in finned tubes. But very few experiments have been done on condensation of CO_2 in micro-fin tubes. Some have been done for other refrigerants.

2. Project description

Some applications need both a low temperature level, harmless and odorless working fluids. CO_2 as a natural refrigerant could be the best solution for this problem when used in a secondary loop of a cascade system.

At this time there are no data available for condensation of CO_2 at low temperatures. As thermophysical properties of CO_2 are in the range of available correlations for conventional refrigerants, heat transfer coefficients of CO_2 at low temperatures can be estimated. Some initial field data predict lower heat transfer at low temperatures. It appears from visualization of CO_2 in smooth tubes, that micro-fin tubes might increase heat transfer at low temperatures.

A test rig has been built to measure heat transfer coefficients in horizontal condenser pipes at low temperatures. A replaceable test section makes it possible to investigate different condenser tube designs including micro-fin tubes. The test section is cooled by a secondary refrigerant circuit, a desired vapor fraction of the two phase flow is generated by an electrical preheater.

Operating conditions including fluid properties are important for the behavior of the flow. In particular, liquid density needs to be relevant since this affects the inertial and gravitational forces of the liquid. The experiments will be carried out with CO_2. Results of this experimental study will be presented as heat transfer coefficient and pressure drop data of CO_2 at varying conditions and vapor fractions. Important conditions during condensation are mass flux, saturation pressure and temperature difference during condensation.

Results of this project might increase the understanding of the mechanisms of two phase flow and help to predict heat transfer in systems important to everyday life. They might even provide a fundament for the construction of new heat exchangers.

3. Theoretical background

3.1 Heat transfer coefficient

Two fluids are separated by a tube wall. One fluid condenses on the inner surface of the tube and releases evaporation enthalpy h_{lv}. This heat is transferred to the wall, conducted through the wall and transferred to a second fluid, the cooling fluid. Figure 3.1 shows a typical temperature profile for a tube wall of a condenser tube.

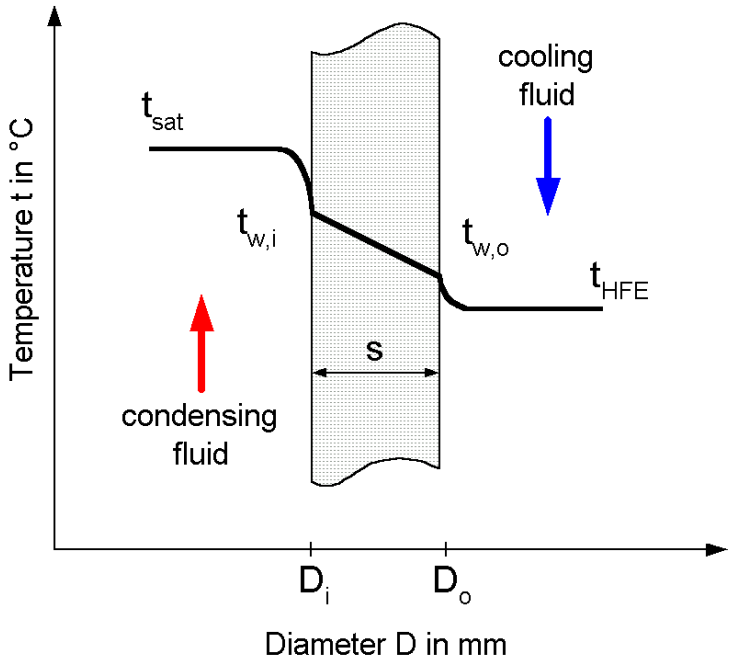

Figure 3.1: Simplified temperature profile of a condenser tube wall.

The heat flow during condensation can be calculated from Equation 3.1.

$$\dot{Q} = \alpha_{eff} \cdot A \cdot (t_{sat} - t_{HFE}) \tag{3.1}$$

Where α_{eff} is the effective heat transfer coefficient, A is the heat transfer area, t_{sat} is the saturation temperature of the condensing fluid and t_{HFE} is the temperature of the cooling fluid. Units of variables and constants are shown in chapter “notations and definitions”. The conjugated total heat transfer coefficient $1/\alpha_{eff}$ is the total thermal resistance and consists of 3 components.

$$1/\alpha_{eff} = 1/\alpha_i + s/\lambda + 1/\alpha_a \tag{3.2}$$

Firstly the condensing heat is transferred to the tube wall. The inner thermal resistance $1/\alpha_i$ results in a temperature difference between the saturated fluid and the inner tube wall. Secondly the heat is conducted through the tube wall with a thickness s and a thermal conductivity λ. The thermal resistance of the tube wall s/λ results in a temperature difference between the inner and the outer tube wall. The third compound of the total thermal resistance is the outer thermal resistance $1/\alpha_o$, that causes a temperature difference between the outer tube wall and the cooling fluid. A reduction in total thermal resistance can be achieved by increased inner and outer heat transfer coefficient, increased

conductivity and reduced thickness of the tube wall. This project analyses the inner heat transfer coefficient that can be calculated from Equation 3.3.

$$\dot{Q} = \alpha_i \cdot A_i \cdot \left(t_{sat} - t_{w,i}\right) \tag{3.3}$$

$\dot{Q}$ can be calculated from the balance of the cooling fluid. Measured values are the inner wall temperature and the inner surface area. For smooth tubes the inner surface area is calculated from the inner diameter, for enhanced micro-fin tubes several inner heat transfer areas are possible which is explained in chapter 5.1.

Reduced thermal resistance may result in four possible improvements:

- Size reduction: If the transferred heat is held constant, the heat exchanger length may be reduced. This provides a smaller heat exchanger and reduces costs of manufacturing.
- Reduced Δt: When heat flow and heat transfer area are held constant, the temperature difference between saturation temperature and temperature of the cooling fluid may be reduced, providing increased thermodynamic process efficiency. As a result operating costs can be reduced.
- Increased heat exchange as reduced thermal resistance is equal to increased heat exchange rate for fixed fluid inlet temperatures and heat exchange areas.
- Reduced compressor power as the heat exchanger can operate at smaller velocities than a heat exchanger with plain surfaces. Higher heat transfer can result in reduced volume flow. Lower volume flow causes less pressure loss in the pipes and the power loss can be reduced proportionally.

3.2 Two phase flow

In gas-liquid flow the two phases can adopt various geometric configurations that are known as flow patterns or flow regimes. According to Whalley [02], important physical parameters in determining the flow pattern are surface tension and gravity. Surface tension keeps the channel walls always wet, unless they are heated during evaporation, and tends to make small liquid drops and small gas bubbles spherical. Gravity tends to pull the liquid to the bottom of the channel in a non-vertical channel.

3.2.1 Flow pattern

Common flow pattern for horizontal flow in a round tube are illustrated in Figure 3.2. As the quality is gradually increased from zero the flow pattern obtained are bubbly flow, plug flow, stratified flow, wavy flow, intermittent and annular flow. Bubbly flow is characterized by small spherical bubbles that tend to flow along the top of the tube and are of approximately uniform size. At plug flow state the individual small gas bubbles have coalesced to produce long plugs. At stratified flow the liquid-gas interface is smooth. Note that this flow pattern does not usually occur, the interface is always wavy as in wavy flow. The wave amplitude increases as the gas velocity increases. Intermittent flow is characterized by a wave amplitude so large that the wave touches the top of the tube. During annular flow the liquid travels partly as an annular film on the walls of tube and partly as small drops distributed in the gas which flows in the center of the tube. Beginning at low quality following flow pattern can be observed.

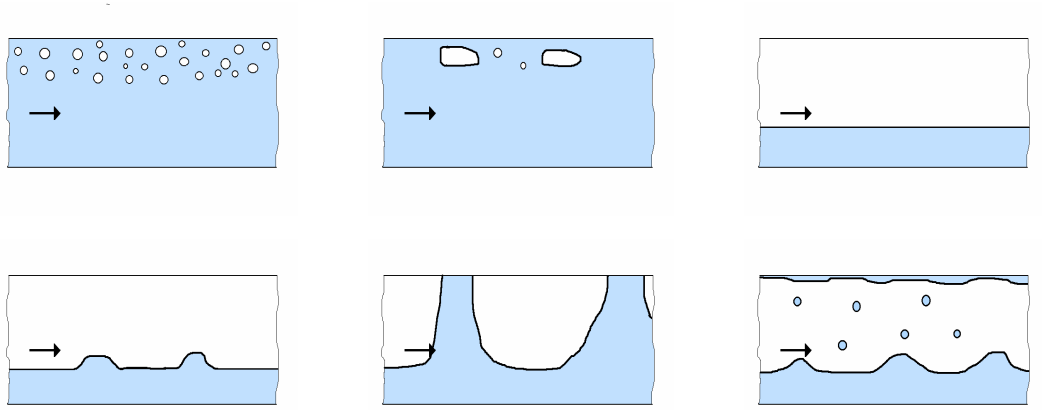

Figure 3.2: Commonly described two phase flow pattern according to Whalley [02].

Many writers define other flow pattern and nearly a hundred different names have been used. Figure 3.2 shows the minimum which can sensibly be defined. Flow pattern of two phase flow are important for heat transfer coefficients and pressure loss. A flow pattern that improves heat transfer during evaporation can reduce the heat transfer during condensation. For example at annular flow conditions during evaporation much higher heat transfer compared to stratified flow conditions can be reached. This is partly due to the fact that at stratified flow the upper inner tube wall is not covered with liquid phase. During evaporation liquid phase covering the inner tube is advantageous for heat transfer. On the other side during condensation the liquid film should be thin for high heat transfer as the thermal resistance of the liquid film reduces the inner heat transfer coefficient.

Annular and stratified annular flows occupy the largest percentage of the length of a condenser. These flow patterns are therefore most important. Chapter 4 and 5 give detailed information about condensation inside horizontal tubes.

3.2.2 Flow pattern determination

The main methods of determining the flow pattern are visualization using a transparent tube and the gamma ray densitometer. Observation by eye is subjective as there are no measured variables. The densitometer measures a mean density across the tube or the average void fraction. This is the proportion of the total volume which is occupied by gas. The results are rarely conclusive and interpretation is subjective too. Such a method has the advantage that it can give results even for flow in an opaque tube.

3.2.3 Flow pattern maps

Flow pattern maps are an attempt, on a two-dimensional graph, to separate the space into areas corresponding to the various flow patterns. Maps can be divided into maps for horizontal flow and maps for vertical flow. Maps for horizontal flow were developed by Baker, Taitel and Dukler 20 Years ago. Development of new flow pattern maps is in progress. Simple flow pattern maps use the same axes for all flow patterns and transitions. For example Kattan's [03] flow pattern map is an enhanced VDI flow pattern map. The VDI map originates from an earlier work by Steiner based on R-12 and R-22. Later on the equations were adjusted to results from experiments with conventional refrigerants like R-134a. A final adjustment to CO_2 was reached by regarding the difference in density of liquid and vapor, viscosity and surface tension of CO_2. The validation of this flow pattern map by

experimental data for CO_2 is not yet done. Yet these maps can be used for the interpretation of the two phase flow. It was therefore used to predict flow regimes for variable refrigerants, tube diameters, tube inclinations towards the horizontal position and saturation temperatures. Figure 3.3 shows an example for a flow pattern map according to Kattan's equations. At this time no flow regime map is available in the open literature that predicts flow pattern inside micro-fin tubes.

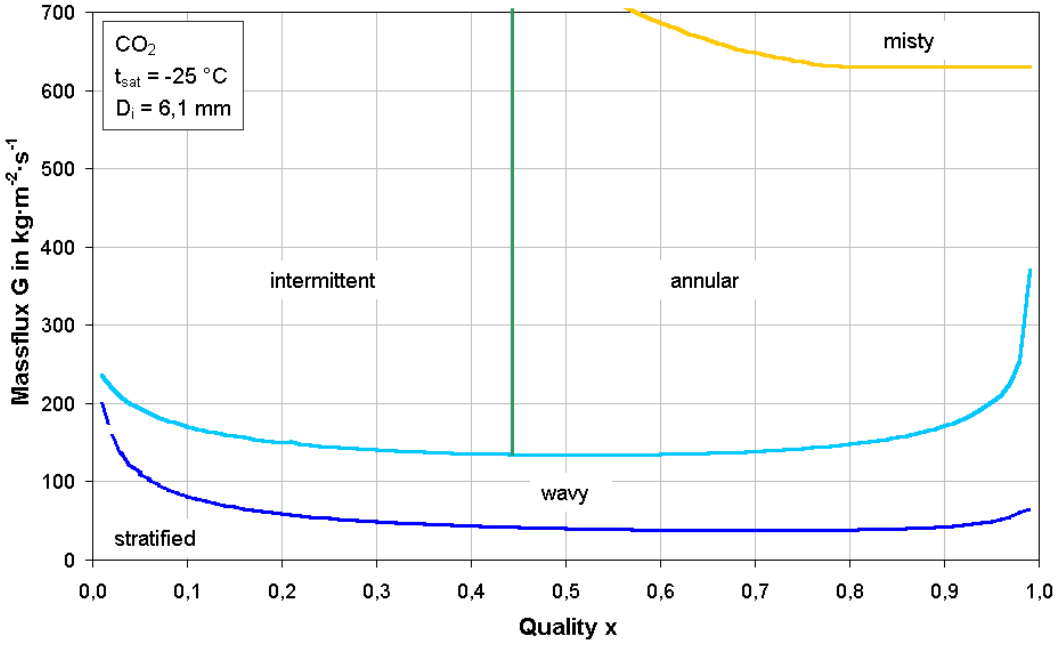

Figure 3.3: Flow pattern map for CO_2 according to Kattan [03]

4. Condensation inside smooth tubes

Heat transfer coefficients (HTCs) are calculated from the Nusselt number. Many correlations to calculate the Nusselt number exist, several were used to calculate and compare HTCs with experimental results. Some correlations were summarized by Dobson et al. [04]. Chapter 4 describes important correlations to calculate inner HTCs for smooth horizontal tubes.

4.1 Gravity driven condensation

At low vapor velocities, gravitational forces which tend to pull condensate down the tube wall are much stronger than vapor shear forces which tend to pull the condensate in the direction of the mean flow. A condensate film forms on the top of the tube and grows in thickness as it flows around the circumference. The bottom portion of the tube is filled with a liquid pool which transports the condensed liquid through the tube in the direction of the mean flow. This heat transfer mechanism is very similar to that in external falling-film condensation. For this reason, heat transfer analysis for gravity driven internal condensation rely heavily on the extensive theory developed for external condensation.

In stratified flow regimes a thick condensate layer flows at the bottom and a thin liquid film is present at the upper portion of the tube. Jaster and Kosky [18] neglect the heat transfer that occurs in the liquid pool at the bottom of the tube and present Equation 4.1. Zivi's void fraction ε is calculated in Equation 4.2.

$$Nu = \frac{\alpha_i \cdot D_i}{k_l} = 0.728 \cdot \varepsilon^{\frac{3}{4}} \cdot \left[\frac{\rho_l \cdot (\rho_l - \rho_v) \cdot g \cdot h_{eq} \cdot D_i^3}{k_l \cdot \mu_l \cdot (t_{sat} - t_w)} \right]^{\frac{1}{4}} \tag{4.1}$$

$$\varepsilon = \left[1 + \frac{1-x}{x} \cdot \left(\frac{\rho_v}{\rho_l} \right)^{\frac{2}{3}} \right]^{-1} \tag{4.2}$$

$$h_{eq} = h_{lv} + 0.68 \cdot c_{pl} \cdot (t_{sat} - t_w) \tag{4.3}$$

To predict the depth of the liquid pool Chato [19] developed a separate model for the flow in the liquid pool based on open channel hydraulics. He showed that, based on conduction only, the heat transfer in the liquid pool was negligible compared to that in the remainder of the tube.

For a constant liquid level in the heat transfer can be approximated reasonably well by the following Nusselt type correlation:

$$Nu = \frac{\alpha_i \cdot D_i}{k_l} = 0.555 \cdot \left[\frac{\rho_l \cdot (\rho_l - \rho_v) \cdot g \cdot h_{eq} \cdot D_i^3}{k_l \cdot \mu_l \cdot (t_{sat} - t_w)} \right]^{\frac{1}{4}} \tag{4.4}$$

4.2 Annular flow condensation

For the annular flow regime, the semi-empirical equations developed by Shah is based on theoretical analysis of the analogy between momentum transfer and heat transfer. For these models the heat transfer coefficient is a function of the interfacial vapor-liquid shear stress and the liquid film thickness.

The most widely cited correlation of the two-phase multiplier type is the Shah [20] correlation. The bracketed term is the two-phase multiplier. It properly approaches 1 as quality x approaches 0, indicating that it predicts the single-phase liquid heat transfer coefficient when all liquid is present. As the reduced pressure is increased, the properties of the liquid and vapor become more alike and the two-phase multiplier decreases. Dobson showed that this correlation is only appropriate for annular flow regimes.

$$\mathrm{Nu} = 0.023 \cdot \mathrm{Re}_l^{0.8} \cdot \mathrm{Pr}_l^{0.4} \cdot \left[1 + \frac{3.8}{p_{red}^{0.38}} \left(\frac{x}{1-x} \right)^{0.76} \right] \tag{4.5}$$

Cavallini and Zecchin [21] used the results of a theoretical annular flow analysis to deduce the dimensionless groups that should be present in an annular flow correlation. They then used regression analysis to justify neglecting many of the groups that did not appear in their empirically developed correlation.

$$\mathrm{Nu} = 0.023 \cdot \mathrm{Re}_l^{0.8} \cdot \mathrm{Pr}_l^{033} \cdot \left\{ 2.64 \cdot \left[1 + \left(\frac{\rho_l}{\rho_v} \right)^{0.5} \cdot \left(\frac{x}{1-x} \right) \right] \right\}^{0.8} \tag{4.6}$$

The bracketed term represents the two-phase multiplier. Cavallini and Zecchin compared their correlation with experimental data from six different studies with R-12 and R-22. The mean deviation between their correlation and the experimental data sets was 30%.

4.3 Boundary layer analysis

The most theoretical approach to annular flow condensation is that of the boundary layer analysis. Traviss' [22] analysis relies on assumptions and simplifications. First of all the velocity profile of the liquid film was extrapolated from the universal velocity profile of single phase flow. Secondly an axisymetric annular film is assumed and any entrainment of liquid in the vapor core flow is neglected. Cartesian coordinates were applied in the liquid film.

$$\mathrm{Nu} = \frac{\mathrm{Re}_l^{0.9} \cdot \mathrm{Pr}_l}{F_2} \cdot \left[0.15 \cdot \left(\frac{1}{X_{tt}} + \frac{2.85}{X_{tt}^{0.476}} \right) \right] \tag{4.7}$$

$$F_2 = 0.707 \cdot \mathrm{Pr}_l \cdot \mathrm{Re}_l^{0.5} \qquad \text{for } \mathrm{Re}_l < 50 \tag{4.8}$$

$$F_2 = 5 \cdot \mathrm{Pr}_l + 5 \ln \left[1 + \mathrm{Pr}_l \cdot \left(0.09636 \cdot \mathrm{Re}_l^{0.585} - 1 \right) \right] \qquad \text{for } 50 < \mathrm{Re}_l < 1125 \tag{4.9}$$

$$F_2 = 5 \cdot \left[\mathrm{Pr}_l + \ln(1 + 5 \cdot \mathrm{Pr}_l) \right] + 2.5 \cdot \ln \left(0.00313 \mathrm{Re}_l^{0.812} \right) \qquad \text{for } \mathrm{Re}_l > 1125 \tag{4.10}$$

Dobson et al. [04] created a new comprehensive correlation covering all flow regimes. His correlation consists of previous correlations that proved to predict HTCs well for one flow pattern. Combination of single correlations with different theoretical and empirical approaches is reached by using conditional terms for mass flux G, Froude number Fr_{So} and Fr_l. The resulting formula expressions are too extensive to be listed here but this correlation sowed to predict HTCs of CO_2 better than correlations for one single flow regime.

4.4 Pressure drop correlation

In designing condensation heat transfer equipment the prediction of pressure drop is as important as the prediction of heat transfer coefficients. Pressure drop during condensation can be obtained from the two-phase flow momentum equation according to Cavallini [08]. The pressure gradient consists of frictional gravitational and acceleration pressure gradients symbolized by subscripts f, g and a. The axial coordinate z is oriented in the flow direction.

$$(dp/dz) = (dp/dz)_f + (dp/dz)_g + (dp/dz)_a \tag{4.11}$$

$$(dp/dz)_g = g \cdot [\varepsilon \cdot \rho_v + (1-\varepsilon) \cdot \rho_l] \cdot \sin(\phi) \tag{4.12}$$

$$(dp/dz)_a = G^2 \cdot \left\{ x^2/(\rho_v \cdot \varepsilon) + (1-x)^2/[\rho_l \cdot (1-\varepsilon)] \right\}/dz \tag{4.13}$$

The gravitational pressure gradient is relevant only for long vertical tubes. The acceleration component which involves a pressure recovery during condensation is often of a comparable amount as the frictional term. For the horizontal adiabatic tube used in the test rig both gravitational and acceleration pressure gradients can be neglected. The frictional pressure gradient in smooth tubes can be calculated with the empirical Equation 4.14. Important variables are mass flux G, inner diameter D_i and mean density ρ_m.

$$\frac{dp}{dz} = G^2 \cdot \frac{75}{2000} \cdot \frac{1}{D_i} \cdot \frac{2000}{\rho_m} \tag{4.14}$$

$$\rho_m = \left(\frac{x}{\rho_v} + \frac{1-x}{\rho_l} \right)^{-1} \tag{4.15}$$

5. Condensation inside micro-fin tubes

Since the end of 1970 condensation heat transfer inside horizontal tubes in heat exchangers is enhanced by finned tubes. Micro-fin tubes play a very significant role in modern high-efficiency refrigerators and air conditioners with their significantly enhanced heat transfer coefficients and low pressure loss characteristics. Low-fin tubes, that are characterized by a fin height hf greater than 0.04 times the inside tube diameter D_{ft}, show high pressure drops and heat transfer coefficients. On the other side micro-fin tubes that have a lower fin height ratio result in high heat transfer coefficients with lower pressure drop. Micro-fin tubes are typically made of copper and have an outer diameter from D_o = 4 mm to 15 mm, a number of fin ranging from nf = 50 to 70 spiral fins with helix or spiral angles from β = 6° to 30°. Usually the fins are triangular or trapezoidal shaped and have a fin height from hf = 0.1 mm to 0.25 mm. Apex angles vary from γ = 25° to 90°. Currently tubes with axial, helical, crosshatched and herringbone patterns are available. This chapter presents definitions for micro-fin tubes, results from earlier studies and correlations for calculation of HTC in micro-fin horizontal tubes.

5.1 Definitions

It is important to define two terms frequently used in the enhanced heat transfer literature: The enhancement factor (EF) and the penalty factor (PF). The enhancement factor is the ratio of the heat transfer in an enhanced tube to that in a smooth tube at the same flow condition. The penalty factor is the ratio of the pressure drop in the enhanced tube to that in a smooth tube at the same flow condition. When micro-fin tubes are used it is important to specify the inner diameter of the tube. Diameters that can be measured are the root diameter D_{root}, at the root of the fins, and the diameter at the fin top D_{ft}. Other often used diameters are the hydraulic diameter D_h, mean diameter D_m and the meltdown diameter D_{melt}. These diameters are superficial and can be calculated only. Figures 5.1 and 5.2 show sketches of a micro-fin tube with important parameters. Measured heat transfer coefficients are dependent on the used inner surface area which in turn is calculated from the inner diameter. The cylindrical envelope surface area of the finned surface at the fin tip is used by Cavallini [08]. Yu and Koyama [09] and Kedzierski and Gonclaves [13] use the actual surface area of the micro-fin tubes.

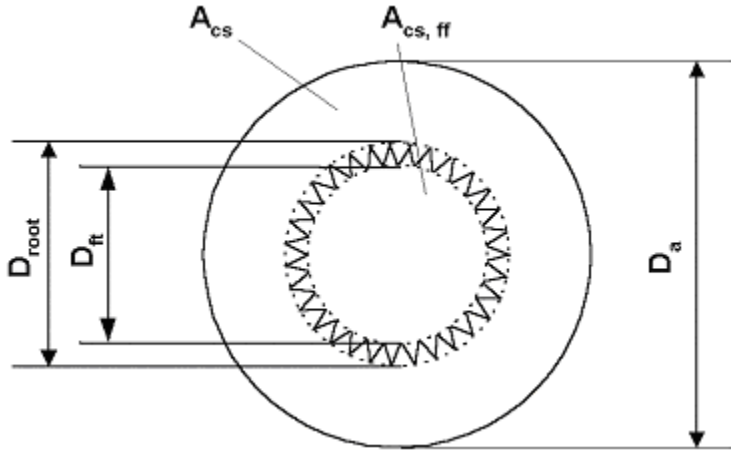

Figure 5.1: Cross sectional sketch of a micro-fin tube.

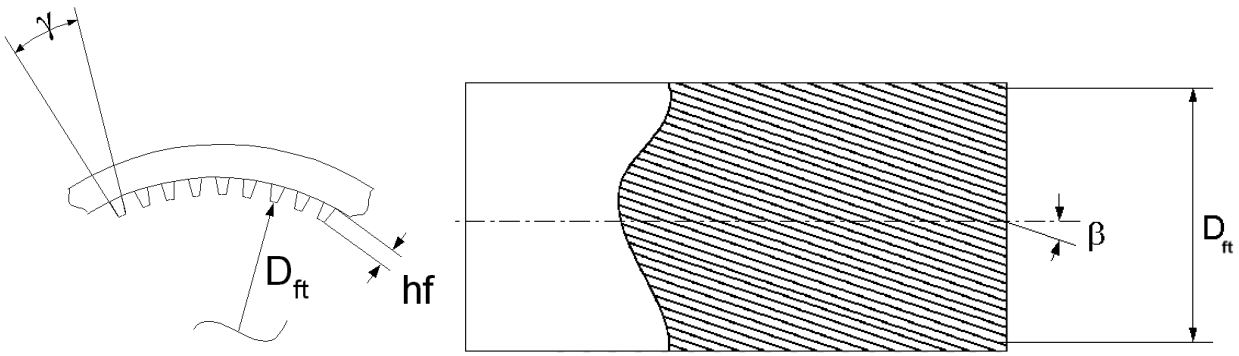

Figure 5.2: Characteristic geometrical parameter of enhanced tubes according to Cavallini [08].

The hydraulic diameter is a superficial diameter of a circle with the same perimeter than the inner perimeter of a micro-fin tube. The inner perimeter is the length of the micro-fin in the cut surface. The length of the inner perimeter is calculated from the profile of the micro-fins. For triangular shaped micro-fins the inner perimeter is calculated by adding the gap between the fins gf to the fin perimeter Pf that is in contact with the refrigerant inside the tube and by multiplying with the number of fins nf. The fin perimeter is calculated from the fin height hf and fin width bf.

$$P_i = nf \cdot (Pf + gf) \tag{5.1}$$

$$Pf = \sqrt{hf^2 \cdot (bf/2)^2} \tag{5.2}$$

The hydraulic diameter is then calculated from Equation 5.3.

$$D_h = P_i/\pi \tag{5.3}$$

This method gives good results for rectangles but gives too high values for the inner diameters of micro-fin tubes. As a result high values for the inner heat transfer area are calculated which in turn results in low values for heat transfer coefficients.

The meltdown method gives much better results. The meltdown diameter is a superficial diameter that would result if the micro-fins were melted down on the inner tube wall. The cross sectional area A_{cs} that is occupied with the tube material is calculated from the outer and the root diameter plus the cross sectional area of the microgrooves.

$$A_{cs} = \pi \cdot D_o^2/4 - \pi \cdot D_{root}^2/4 + nf \cdot Af \tag{5.4}$$

Af is the area of the cross section that is occupied by the material of the fins. Assuming a triangular shape of a fin it can be calculated from the fin height hf and the fin width bf.

$$Af = hf \cdot bf/2 \tag{5.5}$$

The meltdown diameter which is the corresponding inner diameter of a micro-fin tube is than calculated from Equation 5.6.

$$A_{cs} = \frac{\pi \cdot D_o^2}{4} - \frac{\pi \cdot D_{melt}^2}{4} \tag{5.6}$$

The inner heat transfer area is calculated from the meltdown diameter as A_{melt} and the length of the test section.

$$A_{melt} = \pi \cdot D_{melt} \cdot L_{ts} \tag{5.7}$$

The meltdown diameter is used in the calculation routine to calculate heat transfer coefficients and mass flux. Exact parameters of the micro-fin tube used in this study were measured with a microscope and a digital camera. Important information was received from Figure 5.3. Magnification factors range from 5 to 20. As diameters, fin height and apex angle are statistically scattered, mean values were calculated that are shown in Table 5.1.

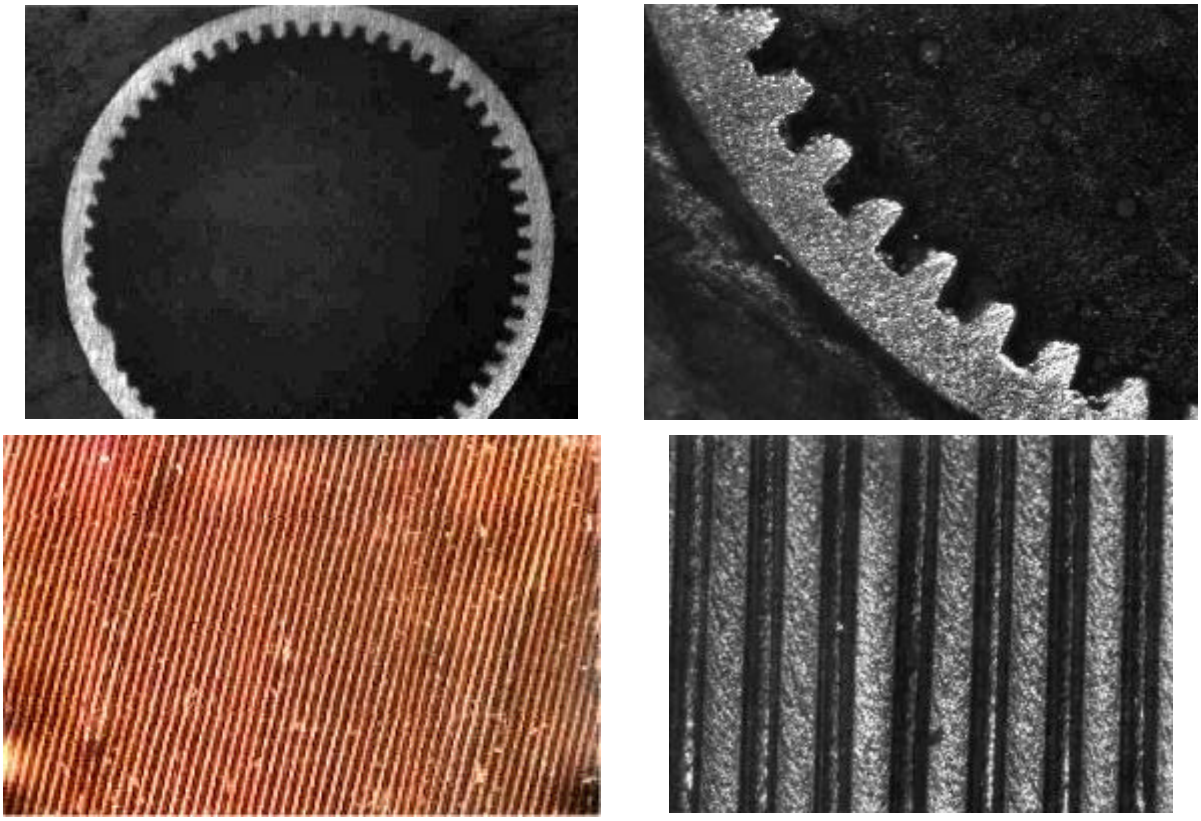

Figure 5.3: Photographs of actually studied enhanced tubes used to measure micro-fin parameters.

Table 5.1: Measured parameters of the studied micro-fin tube.

Parameter	Symbol	Value	Unit
outer diameter	D_o	6,98	mm
root diameter	D_{root}	6,32	mm
diameter at fin top	D_{ft}	5,97	mm
meltdown diameter	D_{melt}	6,26	mm
hydraulic diameter	D_h	9,44	mm
fin height	hf	0,18	mm
fin width	bf	0,12	mm
gap between fins	gf	0,17	mm
number of fins	nf	54	-
inclination angle	β	14	°
apex angle	γ	45	°

5.2 Literature review

Shedd [05] summarized in his Ph.D. thesis important results of previous studies concerning condensation of refrigerants in micro-fin tubes. Measured heat transfer coefficients for R-22 in grooved tubes tend to be 3 or 4 times that in smooth tubes at low mass flux G = 100 to 200 $kg \cdot m^{-2} \cdot s^{-1}$. Condensation of R-22 tends to have penalty factors of PF = 1.5 to 1.8 beginning at low mass flux and increasing at higher mass flux. Evidence from heat transfer data and flow visualization experiments indicates that the enhancement is due to increased wetting of the tube perimeter. Increased effective heat transfer area and turbulence induced in the liquid film by the micro-fins and the surface tension effect in the liquid drainage increase heat transfer coefficients further. It was demonstrated that the fins act to promote the transition from stratified to annular flow at lower qualities and mass flow rates. In addition it was noted that the steady-state film profiles tend to show a rotated symmetry with the thinnest and thickest parts of the film occuring at locations shifted from the top or bottom center in the direction of the fin inclination angle. From these observations it was hypothesized that the fin exerts a stress on the film at the wall in the circumferential direction as a rotating tube would exert. For increasing pressures the enhancement factor became less dependent on mass flux for refrigerants R-22 and R-134a. As pressures are much higher for CO_2 the enhancement factor should be rather independent of the mass flux.

Yang and Webb [06] showed that for R-12 condensate forming on the fin tip is drawn into the groove resulting in high rates of condensation.

Kattan [07] carried out experiments with R-134a at 3.8 °C saturation temperature, tube diameters of 12 mm and mass fluxes of G = 100 to 300 $kg \cdot m^{-2} \cdot s^{-1}$. His experiments gained constant penalty factors of PF = 1.35 and enhancement factors of EF = 4.5 for high mass flux and EF = 1.88 for low mass flux during vaporization.

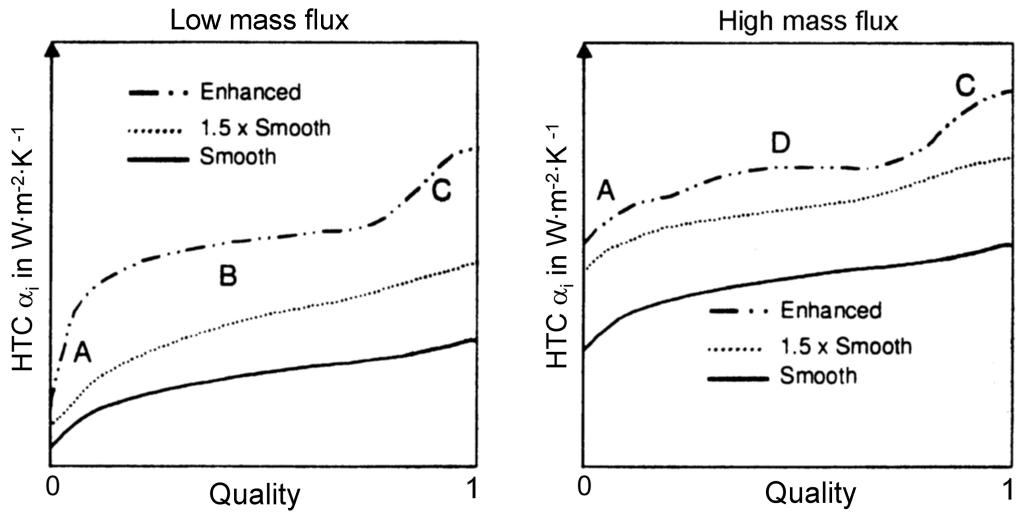

Figure 5.4: Generalized behavior of heat transfer coefficients during condensation according to Shedd [05]. Fluid behavior in the regions marked A, B, C and D is discussed in the following text.

According to Shedd [05] condensation can be divided into three zones depending on mass flux. In each of the zones the micro-fins have a different influence on the heat transfer and pressure drop. Figure 5.4 shows generalized heat transfer coefficients during condensation. The dotted line “1.5 x smooth” shows the approximate enhancement due to the increased surface area of the micro-fin. At the beginning of condensation, quality x = 1, drop wise condensation dominates leading to very high heat transfer coefficients. The micro-fin may reduce the required surface energy for the formation of a droplet as such a droplet can adhere in the v-shaped trench of a fin. The surface of a liquid droplet is then partly covered with two micro-fins and the boundary layer between liquid and gas that requires high formation energy is reduced. The steep decline of heat transfer coefficient marks the beginning of film condensation when the liquid film increases the total thermal resistance. At lower mass flux in region B, due to the lower vapor velocities typical in condensation, the liquid in a smooth tube would tend to fall into a stratified flow. In the helical micro-fin tube some balance of surface tension and shear forces act to significantly enhance the condensation heat transfer. This explains the significant enhancement noted in region B of the low mass flux. Region D of the high mass flux in Figure 5.4 is dominated by annular flow. That the heat transfer remains higher than the surface area increase may be due to the more uniform film distribution allowing more of the tube surface to play an active role in the condensation. In addition the fins appear to affect the wave behavior of the liquid film which could further enhance the heat transfer. A more turbulent liquid film could have higher surface area due to waviness resulting in a better condensation of the gas phase in the center of the tube to the liquid film. As the condensation process nears completion in region A, the heat transfer enhancement approaches that of the percentage increase in surface area plus with some additional enhancement due to capillary or shear forces providing increased wetting of the tube surface. At low mass flux the overall enhancement due to the micro-fin structure is higher than at high mass flux.

5.3 Heat transfer correlations

In his review paper Cavallini et al. [08] presents a correlation to predict heat transfer coefficients during condensation inside low-fin, micro-fin and cross-grooved tubes. It is based on the Cavallini and Zecchin equation for smooth tubes that is presented in Chapter 4.2. It has the form of a forced convection equation and it is fully reported in Table 5.2. The exponents s and t have been derived by Cavallini et al. using a best-fitting procedure from the available experimental data for R-22, R-134a and R-410a. Generally the predicted Nu number was within 20% of Cavallini's experimental data.

Yu and Koyama [09] modified the Haraguchi et al. model for condensation in smooth tubes and presented a new model for condensation of pure refrigerants in micro-fin tubes. This correlation accounts for the effect of inside surface geometry simply by referring the heat transfer coefficient to the total inside heat transfer area. The Yu and Koyama correlation compares well within a 30% range with data from the same authors relative to R-134a, R-123 and R-22.

Table 5.2: Important correlations for calculation of HTC inside horizontal micro-fin tubes.

Reference	Model	Eq. no.
Cavallini et al. [10], [11]	$Nu = \alpha_i \cdot D_{ft} / \lambda_l = 0.05 \cdot R_{eq}^{0.8} \cdot Pr_l^{1/3} \cdot (Bo \cdot Fr)^t \cdot Rx^s$	5.8
	$Re_{eq} = D_{ft} \cdot G_{eq} / \mu_l \quad , \; G_{eq} = M_{eq} / A_{cs,ff} \quad , \; Pr_l = \mu_l \cdot c_{pl} \; / \lambda_l$	5. 9
	$M_{eq} = M \cdot \left[(1-x) + x \cdot \sqrt{\rho_l / \rho_v} \right] \quad , \quad A_{cs,ff} = \pi \cdot D_{ft}^2 / 4$	5.10
	$Rx = \left\{ 2 \cdot hf \cdot nf \cdot [1 - \sin(\gamma/2)] / [\pi \cdot D_{ft} \cdot \cos(\gamma/2)] + 1 \right\} / \cos(\beta)$	5.11
	$Fr = u_{lo}^2 / g \cdot D_{ft} \quad , \quad Bo = g \cdot \rho_l \cdot hf \cdot \pi \cdot D_{ft} / (8 \cdot \sigma_l \cdot nf)$	5.12
	$hf/d_{ft} > 0.04$ then s = 1.4, t = -0.08 $hf/d_{ft} < 0.04$ then s = 2.0, t = -0.26 $Re_{eq} > 15000, \quad 3 < Pr_l < 6.5, \; 0.3 < Bo \cdot Fr < 508, \; 7° < \beta < 30°$	5.13
Yu and Koyama [09]	$Nu = \alpha_i \cdot D_m / \lambda_l = \left(Nu_F^2 + Nu_B^2 \right)^{0.5}$	5.14
	$Nu_F = 0.152 \cdot (\Phi_v / X_{tt}) \cdot Re_l^{0.68} \cdot \left(0.3 + 0.1 \cdot Pr_l^{1.1} \right)$	5.15
	$Re_l = G_{eq} \cdot (1-x) \cdot D_m / \mu_l$	5.16
	$\Phi_v = 1.1 + 1.3 \cdot \left\{ G_{eq}^{0.35} \cdot X_{tt}^{0.35} / [g \cdot D_m \cdot \rho_v \, (\rho_l - \rho_v)] \right\}^{0.175}$	5.17
	$Nu_B = 0.725 \cdot H(\varepsilon) \cdot [Ga \cdot Pr_l / (Ph_l \cdot \eta)]^{0.25}$	5.18
	$Ga = g \cdot \rho_l^2 \cdot D_m^3 / \mu_l^2 \quad , \quad Ph_l = c_{pl} \cdot (T_{sat} - T_w) / h_{lv}$	5.19
	$H(\varepsilon) = \varepsilon + \left\{ 10 \cdot (1-\varepsilon)^{0.1} - 8.0 \right\} \cdot (\varepsilon)^{0.5} \cdot \left[1 - (\varepsilon)^{0.5} \right]$	5.20
	$\varepsilon^{-1} = 1 + [(1-x) \cdot \rho_v / (x \cdot \rho_l)] \cdot \left\{ \frac{0.4 + 0.6 \cdot \left[x \cdot (\rho_l / \rho_v) + 0.4 \cdot (1-x) \right]^{0.5}}{\left[x + 0.4 \cdot (1-x)^{0.5} \right]} \right\}$	5.21

5.4 Pressure drop correlations

Cavallini et al. [08] considered the Sardesai et al. model and the Friedel correlation. The model has been developed for smooth tubes. It can be used for prediction of micro-fin tubes by using a suitable friction factor f. The single-phase friction factor for micro-finned tubes tends to the value for smooth tubes at low Reynolds numbers. At high Reynolds numbers it depends on the ratio of fin height to tube diameter and the fins spiral angle. The correlation has been developed for adiabatic condition as in the pressure loss test section. Computation of acceleration pressure drop requires an evaluation of the vapor void fraction ε.

Kedzierski and Goncalves suggested a different approach to calculate the pressure drop during condensation in micro-fin tubes. Their correlation is based on a semi empirical equation by Pierre for flow boiling inside horizontal tubes and is adjusted to their own data. Other correlations for pressure drop prediction are the Nozu et al. [14] and the Haraguchi et al. [15] model. Both the Cavallini and the Kedzierski and Gonclaves correlation are shown in Table 5.3.

Table 5.3: Important correlations for calculation of pressure drop inside horizontal micro- fin tube.

Reference	Model	Eq. no
Cavallini et al. [12]	$(dp/dz)_f = \Phi_{lo}^2 \cdot (dp_f/dz)_{lo} = \Phi_{lo}^2 \cdot 2 \cdot f_{lo} \cdot G^2/(dp_l)$	5.22
	$\Phi_{lo}^2 = E + (3.23 \cdot F \cdot H)/(Fr^{0.045} \cdot We^{0.035})$	5.23
	$E = (1-x)^2 + x^2 \cdot \rho_l \cdot f_{vo}/(\rho_v \cdot f_{lo})$	5.24
	$F = x^{0.78} \cdot (1-x) \cdot 0.224$, $H = (\rho_l/\rho_v)^{0.91} \cdot (\mu_v/\mu_l)^{0.19} \cdot (1-\mu_v/\mu_l)^{0.7}$	5.25
	$Fr = G^2/(g \cdot D_{ft} \cdot \rho_m^2)$, $We = G^2 \cdot D_{ft}/(\rho_m \cdot \sigma_l)$	5.26
	$\rho_m = \rho_l \cdot \rho_v/(x \cdot \rho_l + (1-x) \cdot \rho_v)$	5.27
	$f_{lo} = \max(f_{lo1}, f_{lo2})$, $f_{vo} = \max(f_{vo1}, f_{vo2})$	5.28
	$f_{lo1} = 0.079 \cdot [G \cdot D_{ft}/\mu_l]^{-0.25}$, $f_{vo1} = 0.079 \cdot [G \cdot D_{ft}/\mu_v]^{-0.25}$ turbulent	5.29
	$f_{lo1} = 16/[G \cdot D_{ft}/\mu_l]$, $f_{vo1} = 16/[G \cdot D_{ft}/\mu_v]$ laminar	5.30
	$(4 \cdot f_{lo2})^{-0.5} = 1.74 - 2 \cdot \log_{10}[2 \cdot e/D_{ft}]$	5.31
	$(4 \cdot f_{vo2})^{-0.5} = 1.74 - 2 \cdot \log_{10}[2 \cdot e/D_{ft}]$	5.32
	$e/D_{ft} = 0.18 \cdot (hf/D_{ft})/(0.1 + \cos\beta)$	5.33
Kedzierski and Gonclaves [13]	$\Delta p = f \cdot G^2 (1/\rho_{out} + 1/\rho_{in}) \cdot L/D_h + G^2 (1/\rho_{out} - 1/\rho_{in})$	5.34
	$f = \{0.002275 + 0.00933 \cdot \exp[hf/(-0.003 \cdot D_{root})]\} \cdot Re^B \cdot \left[(x_{in} - x_{out}) \cdot h_{lv}/L \cdot g\right]^{0.211}$	5.35
	$Re = G \cdot D_h/\mu_l$, $B = (-4.16 - 532 \cdot hf/D_{root})^{-1}$	5.36

6. Experimental facility

An experimental test rig to measure the two-phase heat transfer coefficient under different operating conditions and tube types has been used in this study. The purpose of the test facility is to supply a working fluid to the inlet of the test section at a variety of thermodynamic states ranging from subcooled liquid to superheated vapor. The test section consists of a replaceable condenser tube. Smooth and micro-fin tubes are tested. The outer surface is in contact with a brass layer that is cooled by ether flowing in ten parallel copper tubes. To measure the pressure drop there is a horizontal and a vertical section built up with identical tubes as used in the condenser test section. In addition to the CO_2 cycle there are two refrigerant cycles working with R-404a and one ether (HFE) loop for condensing and subcooling the CO_2. The following chapters will describe the CO_2 loop, the HFE cooling loop, the R-404a loop and the condenser test section in detail.

6.1 CO_2 loop

Figure 6.1 shows a simplified sketch of the CO_2 and the HFE loop. Figure 6.2 shows a simplified structure of the refrigerant cycle in a typical operating point for CO_2. The flow in the loop is driven by a variable speed gear pump (1), saturation temperatures before and after the pump are $t_{P,out}$ and $t_{P,in}$. This is a magnetic pump that is powered by a DC motor which is digitally controlled using a DC transformer to adjust the voltage. Unlike a compressor the gear pump does not require lubrication so the loop can be operated oil-free. In later experiments oil can be added to the refrigerant to study the influence of oil during condensation. Following the pump, the refrigerant mass flow is measured by a coriolis flow meter (Micro Motion CFM25). The CO_2 flow rate can be controlled in three different ways. The most sensitive way of adjustment is to digitally control the AC inverter thus controlling the rotational speed of the refrigerant pump. A second, coarser method is to divert some of the flow through a bypass line around the pump. A third method of controlling the flow is by adjusting the valves in the circuit to provide additional pressure drop and thus reducing the flow. Therefore it is possible to avoid low rotational speeds of the magnetic pump that result in unstable mass flow.

A calorimeter (2) is used to heat the subcooled liquid refrigerant to the desired state at the inlet of the test section. The calorimeter consists of two parallel electrical heaters TRI-5448-240-Omega. According to Figure 6.3 each heater is inside a copper tube with refrigerant flowing through the spirally articulated annulus. The only contact to the outside tube wall is the copper spiral coiled around the heater. Temperature of the outer tube wall is therefore not directly influenced by heat conduction. Both liquid and gas phase have the same temperature when they leave the calorimeter. Additional mixing is reached when both refrigerant flows out of the parallel calorimeter tubes are mixed together head on. Heating capacity of the calorimeter is 3 kW. The power supplied to the heaters is controlled manually with a variable alternating voltage source (variac) and measured by a wattmeter. By adjusting the power to the calorimeter the quality of CO_2 at the test section is regulated.

Exiting the calorimeter the refrigerant flows along a horizontal pipe of 1 m length to establish a flow pattern dependent on mass flux and quality. The condenser test section (3) is a 15 cm long pipe which will be explained in detail in Chapter 6.4. After the test section there is an insulated horizontal and vertical pipe (4), with a length of $L_{ts,ho} = L_{ts,ve} = 1$ m, to measure the pressure loss both in horizontal and vertical flow. This section consists of pipes with identical inner surface and diameter just like the pipe of the condenser test section where heat transfer

coefficients are determined. Differential pressure transducers before and after the horizontal and vertical pipes measure the pressure drop that is used to calculate the penalty factor.

After leaving the pressure loss test section the CO_2 flows through a control heater (5) which evaporates liquid CO_2 in order to keep the pressure of the system at the particular level. This control heater is similar to the calorimeter shown in Figure 6.3. The amount of heat to the control heater is regulated by a PID regulator that uses the pressure measurement as input value. At experiments with high qualities or low mass flow when the liquid flow to the control heater is low, the heater has only little control over the system pressure as it can run dry easily.

System pressure is therefore mainly controlled by the cooling capacity of the main heat exchanger (6). This heat exchanger condenses CO_2 by evaporating R-404a. The main condenser is built at the top of the test rig and the CO_2 outlet pipe leads vertically to the bottom of the test rig. Subcooling in the main condenser is therefore not possible as the liquid phase is immediately pulled out of the heat exchanger by gravity. To get enough subcooling for the CO_2 to run the pump, there is an additional heat exchanger (7) which is cooled by HFE. After being subcooled the CO_2 flows back to the pump. A safety valve adjusted to 450 psi (31 bar) is located in the CO_2 circuit before the gear pump. Operation with CO_2 at higher saturation temperature of t_{sat} = -15 °C requires a buffer volume that is installed by two fade out tanks. Two gas bottles are permanently connected to the refrigerant loop in order to get enough liquid at high temperatures to run the pump. Looking glasses in the vertical pipe before the subcooler make it possible to ensure that the system contains enough liquid phase to be run. A looking glass after the pump allows to ensure a stable liquid mass flow out of the pump. All pipes of the CO_2 loop, calorimeter and test section are insulated by two layers of 1 cm thick insulation foam. A detailed schematic diagram is given by Figure 6.6.

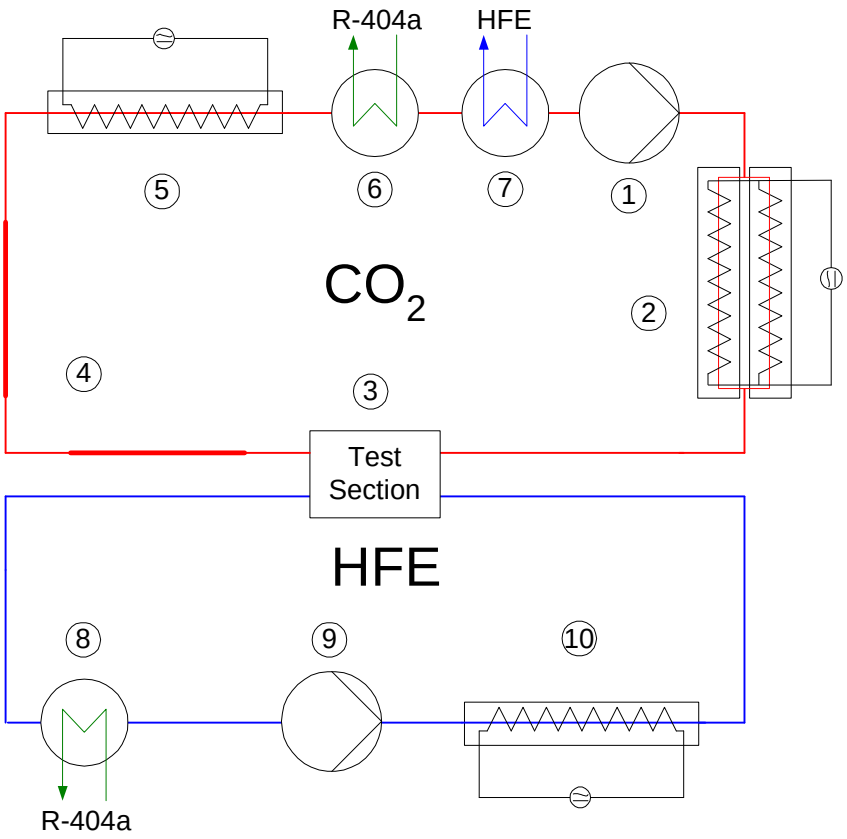

Figure 6.1: Sketch of simplified CO_2 and HFE loop

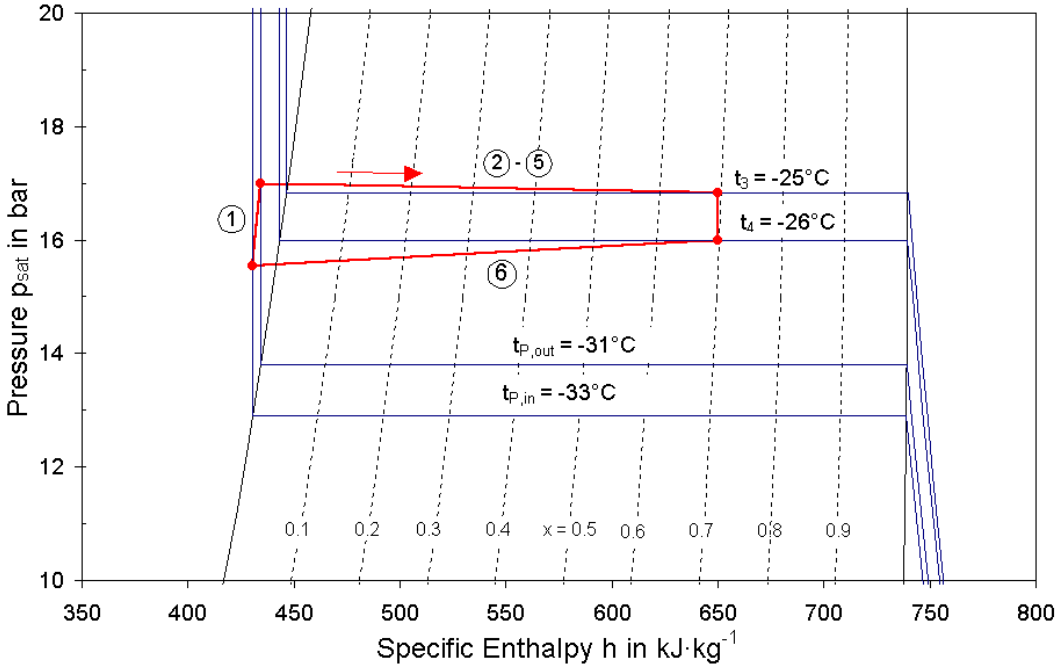

Figure 6.2: Simplified refrigerant loop for CO_2 in p-h-diagram

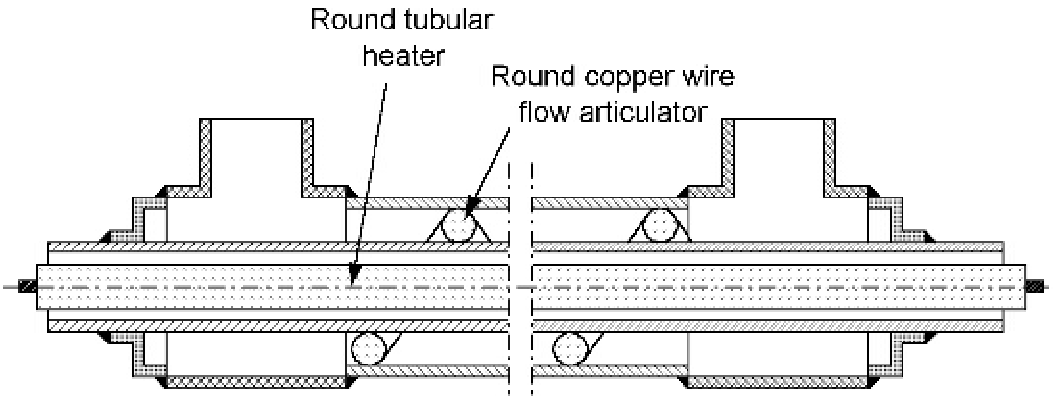

Figure 6.3: Schematic drawing of control heater and evaporator, refrigerant flows around the inner heater pipe and the copper wire.

6.2 HFE loop

The secondary fluid in the cooling loop is HFE – 7100, Methoxynonafluorobutane, an ether compound produced by the company 3M Novec Engineered Fluids. At all conditions in the test rig the HFE is liquid. Figure 6.1 shows the HFE loop with all major components. This HFE is used as cooling liquid for the CO_2 condenser test section. It is also needed to subcool the CO_2 before the gear pump. Heat rejection of HFE is given in a flat plate heat exchanger (8) by vaporization of R-404a that is condensed and compressed by a separate condensing unit. This unit is independent of the R-404a loop for the CO_2 and has a capacity of 1.5 kW and its own thermostatic expansion valve.

The HFE is pumped with a non adjustable pump (9). Coarse adjustment of the HFE mass flow is reached by a bypass around the pump. Fine adjustment is done by a manual valve in the HFE loop. After the pump the flow can be split into two partial flows one for subcooling CO_2 in a flat plate heat exchanger (7) and one for the condenser test section. Splitting is controlled by manual valves. After the two branches rejoin the HFE runs through the filter and dryer in order to remove any water that might remain in the HFE and to filter the fluid. This is necessary since the HFE temperature is below the freezing point of water and small ice particles may affect the flow. The flow is then branched again. One of the branches returns to the R-404a heat exchanger. This branch basically allows the HFE pump to run a high flow rate through the R-404a heat exchanger maintaining a sufficient capacity and at the same time have a variable mass flow through the rest of the loop. The second branch leads to the mass flow meter Micro Motion CFM25.

Immediately following the mass flow meter there is a manual valve which controls the mass flow of the HFE. Following this valve is the HFE heater (10) that allows to adjust the HFE temperature. This heater is similar to the heaters in the CO_2 loop except that there is only one heater for the HFE as opposed to the pair of heaters for the calorimeter. Heating capacity is 1.5 kW. The heater is manually controlled by its own variable voltage source. The HFE then enters the condenser test section where it cools the brass jacket which is explained in Chapter 6.4. After exiting the condenser test section the HFE returns back to the R-404a heat exchanger which finishes the loop. All pipes of the HFE loop are insulated by two layers of insulation to maintain the lowest temperatures at the test rig. HFE temperatures are usually t_{HFE} = -40 °C and lower.

6.3 R-404a loop

Two separate chiller loops are installed. A main chiller for the CO_2 loop and a chiller for the HFE loop. The purpose of the R-404a loop is to supply definite cooling capacity to transfer the required heat from the CO_2. The R-404a loop for cooling and condensing the CO_2 vapor consists of a Copeland condensing unit model 3DB3-100L-TFC-220 with a capacity of 8 kW at an evaporation temperature of -40 °C and a condensation temperature of 30 °C and two heat exchangers. The compressor is driven by a variable speed motor that can be adjusted by a digital controller. Further adjustment of cooling capacity is reached by a thermostatic expansion valve and a manual valve. The R-404a evaporates in a flat plate heat exchanger, (6) in Figure 6.1, the vaporization energy is received by condensing CO_2 at the other side of the heat exchanger. Adjustment of cooling capacity is important to keep a specified pressure in the CO_2 loop.

For cooling of HFE and subcooling of CO_2 an additional Copeland chiller model KWLB-015E–CAV is installed. According to a condenser capacity chart of a similar condensing unit the capacity is above 1.5 kW for a R-404a evaporation temperature of -30 °C and a condensing temperature of 30 °C. R-404a evaporates in a flat plate heat exchanger (8) and cools the HFE loop. Both chillers are cooled by tap water. For higher cooling capacity chilled water from the building supply can be run through the heat condensers the R-404a loops.

6.4 Test section

The test section consists of a condenser test section to measure heat transfer coefficients and to calculate the enhancement factor. A horizontal and a vertical pipe are installed in order to measure the pressure loss in smooth and micro-fin tubes and to calculate the penalty factor.

In the condenser test section the CO_2 flows through a 25 cm long pipe with an inner diameter of $D_i = 6.1$ mm for the smooth tubes, a length of $L_{ts} = 0.15$ m of that pipe are surrounded by a brass jacket. For the inner surface of a micro-fin an equivalent inner diameter is calculated as explained in Chapter 5.1. In that short pipe the quality x changes only by $\Delta x = 0.01$ at most which allows to measure heat transfer coefficients at definite qualities reaching from $x = 0.1$ to $x = 0.9$. The outer diameter is $D_o = 9.6$ mm. A micro-fin tube consists of an inner copper tube that contains micro-fins at the inner surface. The inner tube is soldered into an outer copper tube. Twelve thermocouples are soldered into three times four millings uniformly distributed at the outer tube. The inner pipe of the condenser test section is surrounded by a brass jacket. The cooling fluid HFE flows around this jacket in copper pipes according to Figure 6.4. The brass envelope provides a uniform temperature profile for condensation and compensates for temperature fluctuations of the HFE stream. As the piping of HFE is important for a uniform condensation temperature it is explained in detail. First the flow is branched to the back and front of the brass jacket. The branch at the back leads to eight parallel sub-branches going over the top to the front of the brass jacket. Each sub-branch then connects to a single pipe that combines the eight flows. Directly underneath this pipe is the front branch which has eight sub-branches going from the front to the back traveling underneath the brass jacket. The sub-branches connect to a flow combining pipe running along the back underneath the back branch. The two combining pipes join afterwards to continue the flow.

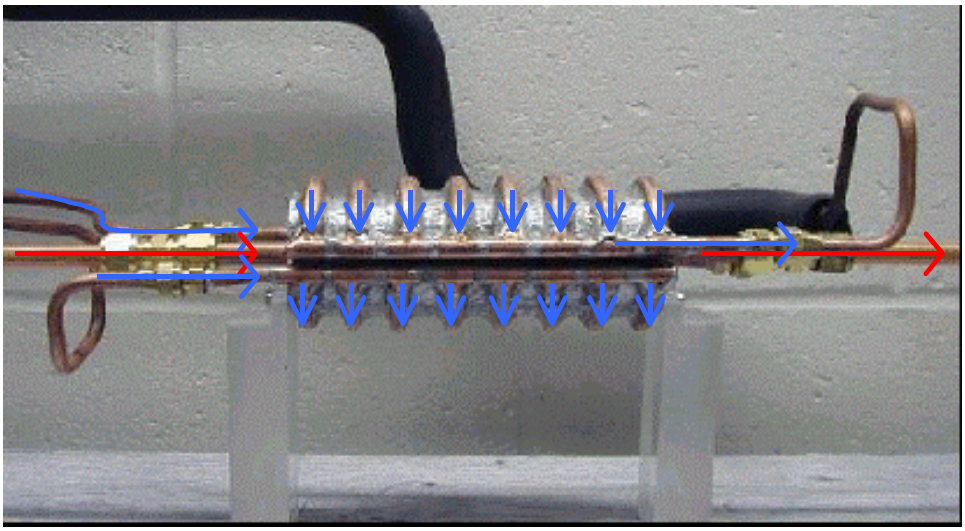

Figure 6.4: Picture of condenser test section with CO_2 and HFE flow directions.

Figure 6.5 shows a cross sectional representation of the test section and a temperature profile. The wall temperature is measured at the bottom of the grooves in the inner tube. As the grooves are 1 mm deep the residual wall thickness is s = 0.85 mm. Radial heat conduction results in a temperature difference between the thermocouples compared to the inner wall temperature of $\Delta t_{w,i,o}$ = 0.1 K. This temperature difference is neglected because it increases the measured heat transfer coefficient by 0.3% at maximum. Two thermocouples measure the HFE temperature entering the condenser test section and the HFE temperature after the condenser test section.

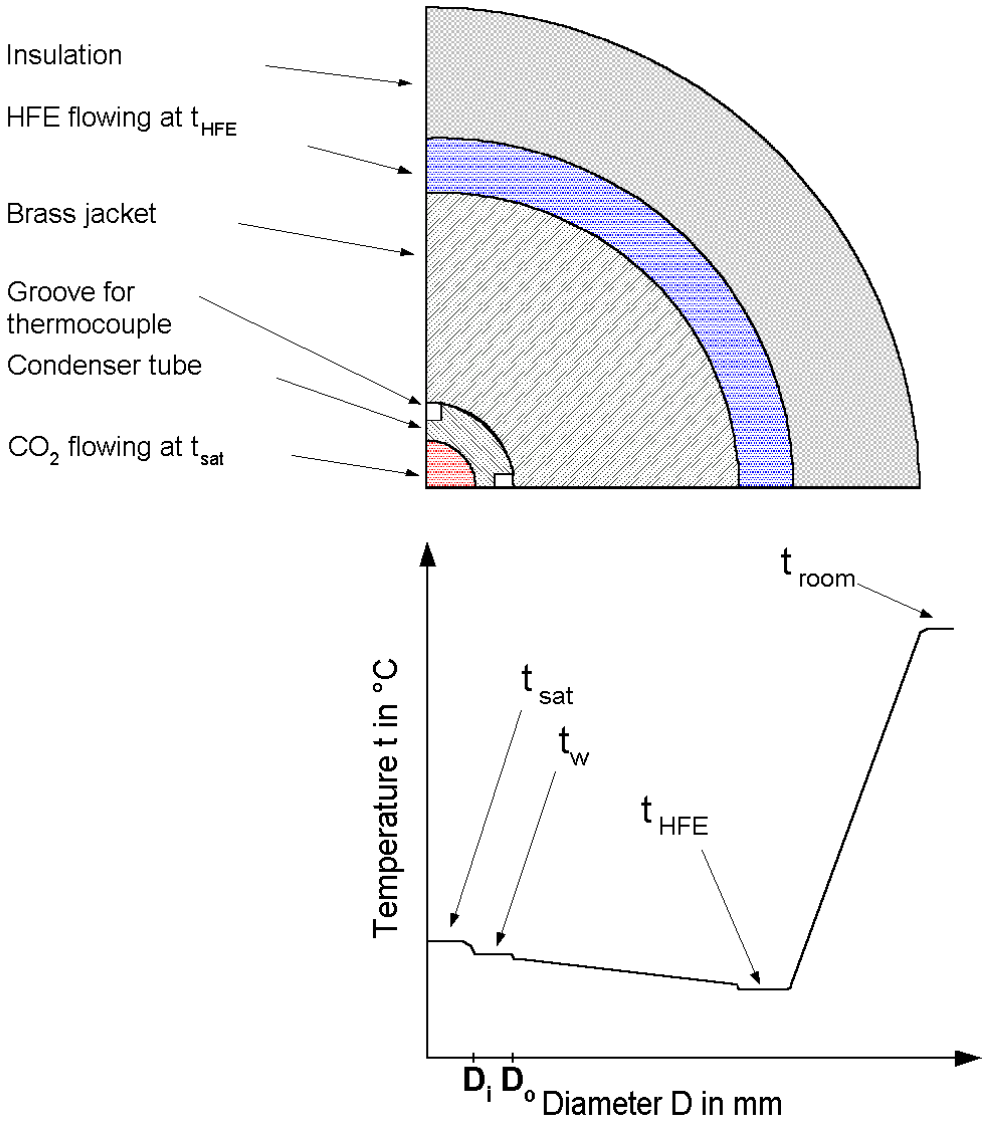

Figure 6.5: Non true scale cross sectional representation of condenser test section with a typical temperature profile.

The complete experimental facility shown in Figure 6.6 consists of two main loops. The CO_2 loop is shown in red and the HFE loop is shown in blue. The CO_2 and the cooling fluid exchange heat at the condenser test section. Both fluids are cooled by separate R-404a loops shown in green. Notice that there is an evaporator test section left in Figure 6.6 that allows measurement of evaporation heat transfer coefficients. This evaporator test section can be used in future studies but was not used during this research.

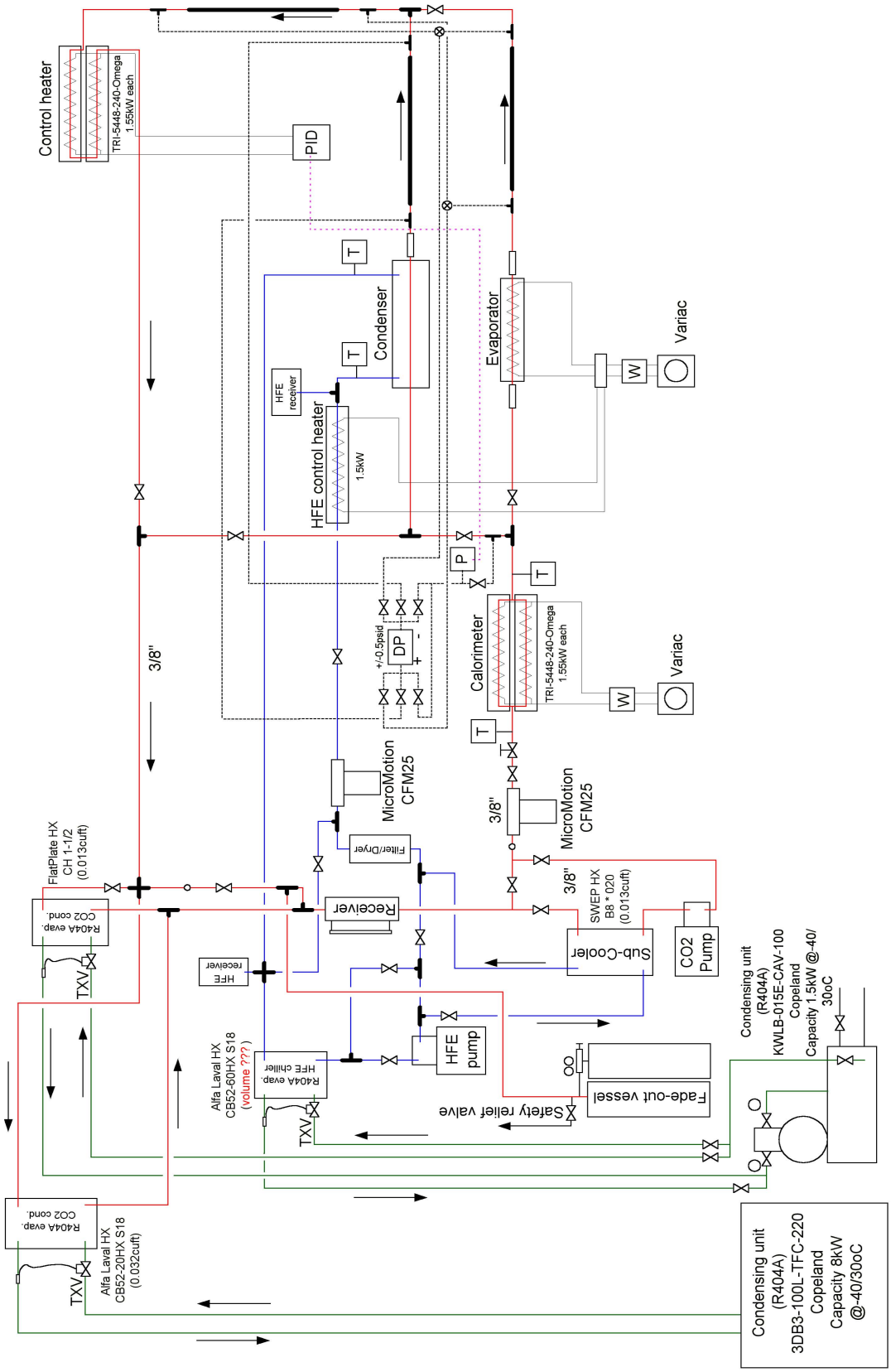

Figure 6.6: Functional diagram of experimental facility

6.5 Instrumentation

Measurement devices used in this study include thermocouples, absolute and differential pressure transducers, flow meters and watt transducers. These devices are discussed in this chapter. Detailed uncertainties of measurement devices are discussed in Chapter 8.

For all temperature measurements in this study thermo-coax, copper-constantan thermocouples were used. The reference temperature of the datalogger which is room temperature is used as reference temperature for the measurements. Ice as reference temperature may be inaccurate because the melting-freezing point of local tap water is not exactly 0 °C.

At the CO_2 loop thermocouples are mounted before and after the calorimeter to be able to calculate the enthalpy of subcooled CO_2 at the inlet of the calorimeter. A thermocouple at the outlet of the calorimeter assures that two phase state is reached. Twelve thermocouples at the test section give a mean value of the wall temperature of the condenser tube.

At the HFE loop two thermocouples before and after the test section are needed to calculate the heat flow $\dot{Q}_{HFE}$. Most critical temperature measurements are those at the HFE inlet and outlet of the test section since they determine the heat transfer rate for the two-phase experiments. As the CO_2 balance around the test section is not possible, there is only the HFE balance to calculate the heat flow. To ensure accuracy of the HFE balance the measured temperature difference between outlet and inlet temperature at the test section has to be at least $\Delta t_{HFE} = 1.5$ K in order to keep the relative error in temperature difference low.

Absolute pressure in the refrigerant loop is measured with a pressure transducer type Sensotec model THE 3883-06TJA. Pressure readings can be switched to four pressure taps. Locations of pressure taps are after the calorimeter, directly after the test section, after the horizontal and after the vertical test section. Pressure range is 0 to 33 bar. Saturation pressure at a typical test run with CO_2 at $t_{sat} = -25$ °C is $p_{sat} = 17$ bar. All thermo physical properties of CO_2 are based on the pressure reading after the test section. Pressure values of this transducer are used to give input values to the PID regulated control heater. During single-phase testing it is also used to compute the refrigerant enthalpy from the equations of state.

Differential pressures are measured around the horizontal and vertical pressure loss test section with a Sensotec pressure transmitter model 7/5556-06. It measures differential pressure from -5 PSI to +5 PSI ($\pm$ 0.34 bar).

Electrical power inputs to the calorimeter and to the HFE heater are measured with watt transducers. The installed watt transducers are OSI precision AC transducers model GW5. GW5-021X5 is installed for the calorimeter and GW5-011X5 for the HFE heater. Power range is 0 to 4 kW for the HFE heater and 0 to 8 kW for the calorimeter.

The refrigerant and HFE mass flows are measured with Elite Micro Motion mass flow meters. The meters are connected to signal converters. Minimum mass flow that can be measured with acceptable relative error is $\dot{m}_{HFE} = 4$ g·s^{-1}. Nominal mass flow range for CO_2 and the HFE mass flow meters is 0 - 300 g·s^{-1}. CO_2 mass flows at experiments range from 5 g·s^{-1} to 13 g·s^{-1}.

The data are processed using a Campbell Scientific datalogger model CR23X Micrologger. The multiplexer changes between the different input channels while the multimeter measures the voltage, digitizes and sends it to a

PC. In the PC the data are processed using a dedicated program that converts the voltage and current signals to physical quantities. This processing is done by the program PC208W written by Campbell Scientific. This program continually writes a text file with all measurement data to the fixed disk of the personal computer. Further data processing and calculation procedure are explained in Chapter 7.1.

7. Experimental Procedures

This chapter describes the procedures used to collect and analyze experimental data. Section 7.1 discusses preliminary operation of the experimental facility including preparation of the facility. Chapter 7.2 and 7.3 describe the procedures to ensure the reliability of experimental data. Section 7.4 describes the methods used to calculate quality of two-phase flow, transferred heat and heat transfer coefficients from raw data. This chapter also includes selected analysis to correct experimental errors.

7.1 System operation

Operation of the experimental system was preceded by a series of rigorous procedures to ensure the integrity of experimental data. These procedures including leakage testing, system evacuation and the start up procedure are followed by a discussion of the procedures used to collect two-phase flow data.

After a new tube geometry is installed or after testing with a particular refrigerant is completed it is necessary to find and remove all leakages. This is done by pressurizing the refrigeration loop with Nitrogen instead of CO_2 because CO_2 may re-sublimate or freeze at a leakage and block it, thus making it impossible to detect the leakage. After removing the insulation from all potential leakages, couplings and valves, a liquid leak detector is used to find leakages. A leakage is found when bubbles occur and grow at a coupling or valve. Leakages can be closed by tightening a screw joint. When screw joints are tightened to strong a plastic deformation in addition to the normal elastic deformation occurs and the joint will permanently leak when opened the next time. According to this effect, a deformation of the inner diameter of the tube may occur which disturbs the flow pattern and increases the pressure drop. Pressure and its change over time are recorded by the data logger over a long period and give a relative answer on how tight the system is.

When all leakages are removed and the insulation is reapplied Nitrogen or any other non- condensable faulty gases in the refrigeration loop have to be removed by evacuation. A vacuum pump that is connected to the cycle reduces the pressure inside the cycle to a very low pressure. As the pressure cells for CO_2 are designed to measure high pressures, the vacuum pressure cannot be measured correctly. But the tendency of pressure change is logged and displayed as a function over time. When a minimum, constant pressure is reached a vacuum is assumed. Additional pressure measurement at the vacuum pump ensures a vacuum. Vacuuming time for the test rig is roughly 1 hour. After vacuuming, the system is pressurized with CO_2 and vacuumed again to minimize the concentration of any faulty gasses. Then the refrigeration cycle has to be filled and pressurized instantly with CO_2 to get a stable pressure above environmental pressure.

To start the refrigerant system the computer system and data logger need to be started and connected to be able to check temperatures and pressures. Before the water cooled chillers can be turned on they need to be supplied with water. Cooling media is tap water which has a temperature of 10 °C in winter times. A main power switch supplies the chillers and pumps of the test rig with electricity.

To ensure heat removal of the test rig; the two water cooled R-404a chiller systems and the HFE pump are activated. The main chiller system cools and condenses CO_2, the HFE chiller system cools HFE that on the other hand is required to subcool the CO_2. When the chillers and the HFE pump are turned on the gaseous CO_2 circulates to the condenser and accumulates at the lower pipes of the test rig as liquid phase. When there is pure liquid at

looking glasses above the subcooler, the CO_2 gear pump is turned on. Stable mass flow is controlled at a looking glass after the CO_2 pump. When the CO_2 flow is stable calorimeter and control heater are turned on to adjust a definite saturation pressure and vapor fraction. When these heaters are active it is important to sustain the CO_2 mass flow otherwise the heaters can burn. To prevent burning of the heaters two thermal control switches for each heater are connected to its power supply. These security switches measure the heater temperature and disconnect the power supply when the maximum temperature is exceeded.

When the pressure has reached the definite level the calorimeter is set to generate a definite CO_2 quality at the test section inlet with the current mass flow. The amount of heat needed is calculated from the subcooled state before the calorimeter inlet using a program routine. Another important parameter to adjust is the wall temperature at the inner diameter of the test section. As the saturation temperature of the CO_2 two phase flowing inside the test section is fixed at fixed pressure, the temperature and mass flow of HFE flowing at the outside of the test section are regulated, see Figure 6.5. Adjustment of HFE mass flow is achieved by tuning the bypass around the HFE pump, bypass around the CO_2 subcooler and the bypass around the test section. A valve before the test section can also be closed to produce additional pressure drop. HFE temperature can be reduced by increasing the mass flow through the R-404a heat exchanger the temperature can be increased by adjusting the HFE heater.

After the software has connected the data logger to the computer, the data logger continually writes data to a text file. After a steady state is reached the text file is deleted and a new one with the steady state data is written for 15 minutes. Every 5 seconds one data point is written to the memory of the data logger. Every minute the data are transferred to the computer. Later the text file with 180 data points is imported into an excel worksheet where mean values are calculated and calibration values are applied. Data are checked for inconsistence with an excel graph.

The mean values are then copied to the program Engineering Equation Solver (EES) that is able to process data and solve equations without strict order for sequence and syntax. It also runs iterations.

7.2 Experiments with R-22

In order to ensure the integrity of the test rig, it was filled with R-22. Much data about heat transfer coefficients for that commonly used old refrigerant exist. Correlations by Dobson, Cavallini and Shah explained in chapter 4 are based on experimental results for refrigerants like R-134a and R-22. Measured heat transfer coefficients from the test rig using R-22 must correspond with such correlations. Experiments are implemented to measure the heat transfer coefficients during condensation of R-22 in a smooth tube with an inner diameter of D_i = 6.1 mm. Experimental conditions were chosen which are important for later experiments with CO_2. The mass flux was set to G = 400 $kg \cdot m^{-2} \cdot s^{-1}$. Heat transfer coefficients which should be independent of the temperature difference as the Equation 7.4 should yield the transferred heat with α_i as a constant for a fluid at specific pressure and flow conditions.

Most interesting are the results of the measurements at the saturation temperature of t_{sat} = -20 °C, as experiments with CO_2 will be done at low temperatures of t_{sat} = -25 °C and t_{sat} = -15 °C. Figure 7.1 shows measured HTC at varying quality for R-22 at t_{sat} = -20 °C and at Δt = 3 K and Δt = 6 K temperature difference between wall and saturation temperature during condensation. The data clearly show that the raw, uncorrected HTCs for Δt = 3 K

temperature difference are higher than HTCs for $\Delta t = 6$ K temperature difference. The graph also shows a set of corrected data that are independent of temperature differences. Four possible errors can lead to these erroneous results:

- A pressure drop in the test section could result in a wrong pressure reading after the test section. This pressure drop is proven to be negligible as two p-t curves of R-22 were created, one at high mass flow and one at zero mass flow. The two p-t curves were identical. A pressure drop that is proportional to the mass flow can be excluded therefore.
- The twelve thermocouples at the test section are calibrated relative to each other. Absolute calibration is unsure as the melting point of ice from local tap water, that is not exactly zero degree, was used for the calibration.
- Another explanation is an imperfect purity of the refrigerant that could cause an imperfect p-t curve.
- Finally the pressure measurement could be inaccurate.

All four possible errors can be excluded using a new p-t curve, different from the p-t curve of a pure refrigerant. Chapter 7.3 explains the procedure to correct for these possible inaccuracies of pressure and temperature measurement and purity of the refrigerant. All procedures for R-22 have been reapplied to the CO_2.

Corrected HTC shown in Figure 7.1 correspond well with correlations. Also the difference between HTC at $\Delta t = 3$ K and $\Delta t = 6$ K temperature difference is corrected for.

Figure 7.2 shows HTCs at $t_{sat} = 10$ °C saturation temperature. HTCs are independent of temperature differences. Compared to predicted HTCs the measured data follow the trend but are consistently lower.

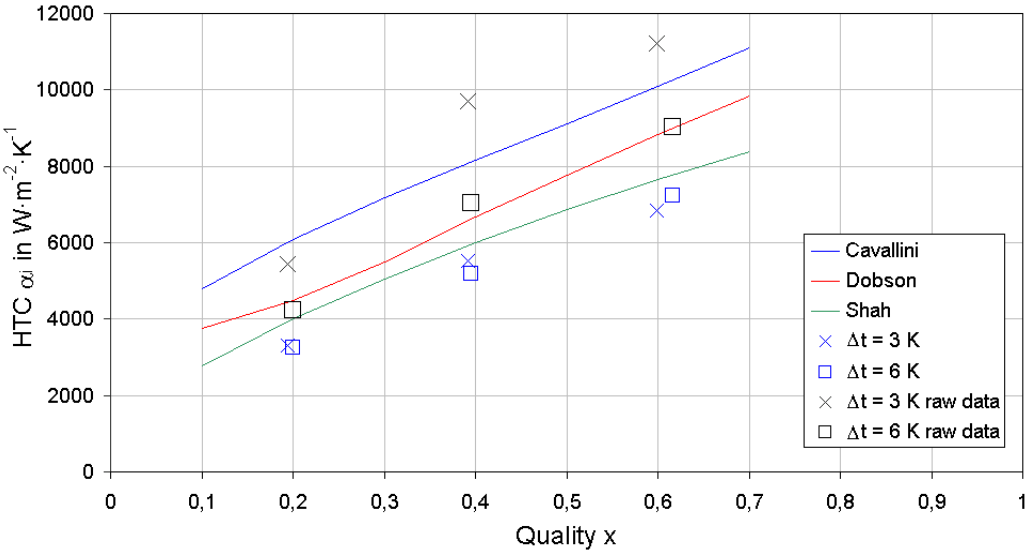

Figure 7.1: Comparison of heat transfer coefficient of R-22 at varying quality x with correlations at $t_{sat} = -20$ °C and $G = 400$ kg·m^{-2}·s^{-1}. Note that $\Delta t = t_{sat} - t_{w,i}$.

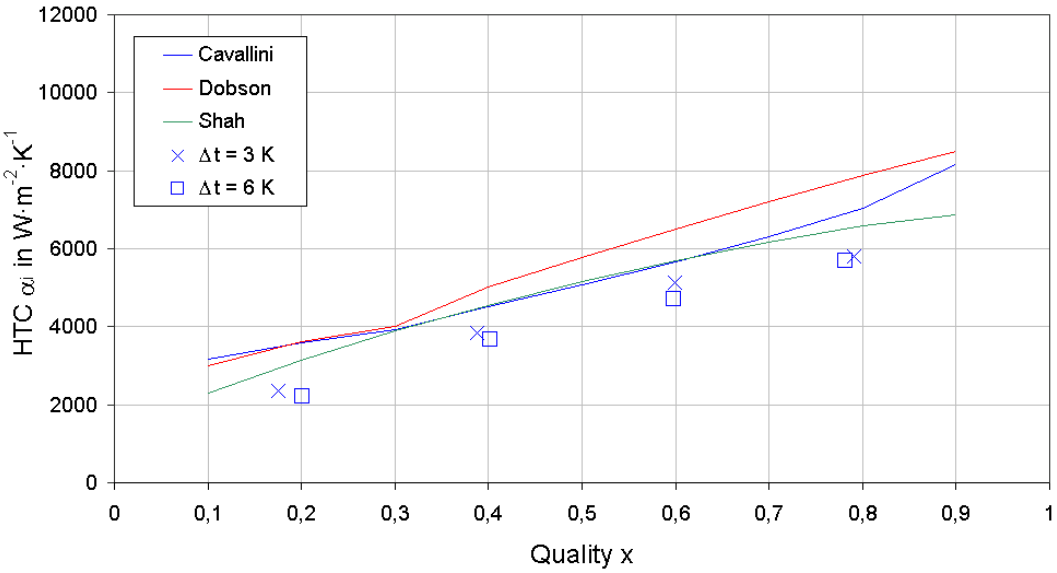

Figure 7.2: Comparison of heat transfer coefficient of R-22 at varying quality x with correlations at t_{sat} = 10 °C and G = 400 kg·m^{-2}·s^{-1}. Note that $\Delta t = t_{sat} - t_{w,i}$.

The new p-t relationship for CO_2 is shown in Figure 7.3. Equation 7.3 applies a polynomial least square fit to the test data that gives an equation for the corrected p-t curve for CO_2. The corrected p-t curve is given by Equation 7.3 and shown as the blue line. Figure 7.3 also shows three data points recorded at high mass flux to ensure applicability of the corrected p-t curve. The measured p-t curve for CO_2 is shifted upwards compared to the real p-t curve according to "REFPROP 6". Whereas the measured p-t curve for R-22 that is not shown here crosses the theoretical p-t curve for R-22.

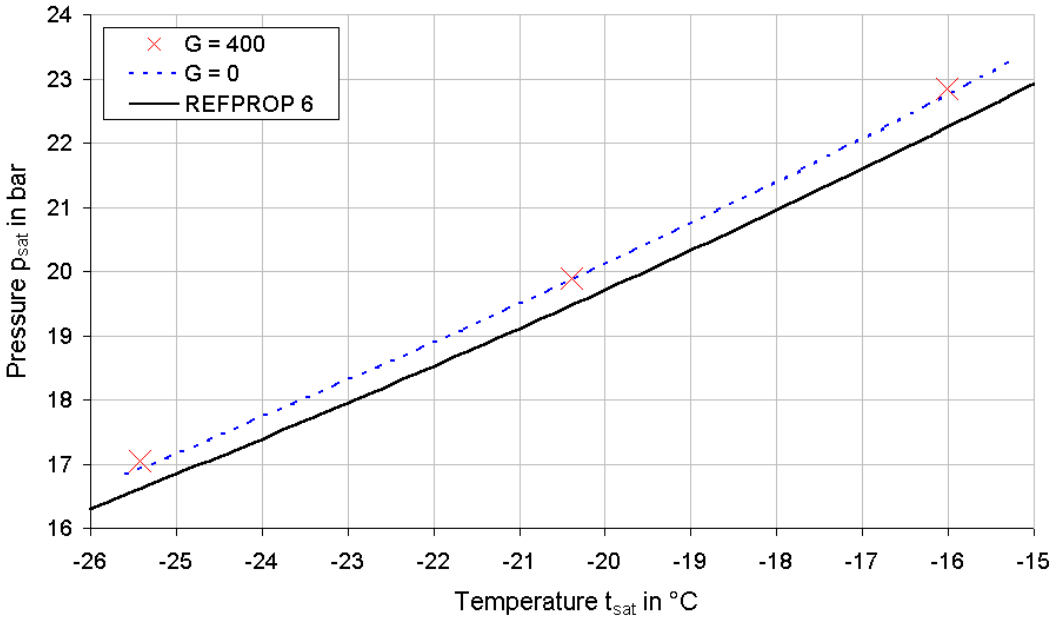

Figure 7.3: Corrected p-t curve and p-t curve according to "REFPROP 6" for CO_2. Note that G is in kg·m^{-2}·s^{-1}.

7.3 Calibration of thermocouples

The twelve thermocouples at the test section wall and the pressure cell that measures the pressure directly after the test section, are calibrated separately. Measurements with R-22 showed that the p-t relationship of measured pressure and measured temperature does not exactly result in the p-t curve for R-22. This p-t curve is calculated using equations of state of "REFPROF 6" that is integrated into the EES program and is currently used at the University of Illinois. In addition the p-t curve of "REFPROP 6" was compared with the p-t curve calculated from equations of state that are used by "SINTEF Energy Research" and found to be identical. It is therefore necessary to calibrate the temperature reading to the pressure reading in order to get a corrected p-t curve.

To create the p-t curve the test rig was cooled down by the R-404a cooling loop and subsequently slowly heated up to room temperature due to heat transmission from the environment. Saturation pressure was measured at a high altitude at the test rig to be sure to measure within the gas phase and to exclude pressure differences due to a possible liquid column. Saturation temperature was measured in the liquid phase for higher accuracy. From the recorded saturation pressure and saturation temperature a p-t curve was created and printed in Figure 7.3.

To calculate a new p-t relationship from the data points a best fit method of least squared errors according to Stoecker [16] is applied. The squared difference between measured saturation temperature t_{sat} minus calculated saturation temperature $t_{sat,calc}$ for m measurement points is minimized by calculation the coefficients a, b and c.

$$\sum_{i=1}^{m}\left(t_{sat,\,i}-t_{sat,\,calc,\,i}\right)^2=\sum_{i=1}^{m}\left(t_{sat,i}-(a\cdot p_{sat,i}^2+b\cdot p_{sat,i}+c)\right)^2 \tag{7.1}$$

Differentiating partially with respect to a, b and c results in three linear simultaneous equations expressed in matrix form.

$$\begin{bmatrix} m & \sum p_{sat,i} & \sum p_{sat,i}^2 \\ \sum p_{sat,i} & \sum p_{sat,i}^2 & \sum p_{sat,i}^3 \\ \sum p_{sat,i}^2 & \sum p_{sat,i}^3 & \sum p_{sat,i}^4 \end{bmatrix}\begin{bmatrix} a \\ b \\ c \end{bmatrix}=\begin{bmatrix} \sum t_{sat,i} \\ \sum p_{sat,i}\cdot t_{sat,i} \\ \sum p_{sat,i}^2\cdot t_{sat,i} \end{bmatrix} \tag{7.2}$$

A program was written to calculate a, b and c for 700 measurement points resulting in a new p-t relationship. With the measured saturation pressure of p_{sat} in kPa it is possible to calculate the measured saturation temperature t_{sat} in °C.

$$t_{sat}=-0.000003248\cdot p_{sat}^2+0.02907\cdot p_{sat}-65.33 \tag{7.3}$$

To verify the p-t relationship at high mass flux following procedure was applied. Figure 6.5 shows a non true scale cross sectional representation of the condenser test section. In the center is the condenser tube with CO_2 flowing inside. The temperature t_{sat} is the saturation temperature according to the measured saturation pressure p_{sat}. Twelve thermocouples in the wall of the copper condenser tube measure the inner wall temperature. In order to ensure equality of wall temperature and saturation temperature, the HFE temperature is adjusted to the CO_2 temperature. As one can see from Figure 6.5 the thick brass jacket results in a temperature slope that strongly reduces the temperature difference between the saturation temperature and wall temperature. In addition the thermal inertness of the brass jacket compensates for temperature fluctuations. This procedure allows to claim the wall temperature to be saturation temperature and to calibrate the wall thermocouples to the pressure transducer. Figure

7.3 shows that the measurement points at high mass flux are on the corrected p-t curve, created from data points at zero mass flux.

7.4 Calculation of heat transfer coefficient

7.4.1 Important balances

The overall heat transfer coefficient HTC is determined from the standard expression given in Equation 7.4. The saturation temperature t_{sat} is calculated from the measured saturation pressure p_{sat} using the corrected p-t relationship given in Equation 7.3. The heat flow $\dot{Q}_{CO2}$ is obtained from the HFE balance given in Equation 7.5 and Equation 7.6.

$$\dot{Q}_{CO2} = \alpha_i \cdot A_i \cdot \left(t_{sat} - t_{w,i,ts}\right) \tag{7.4}$$

$$\dot{Q}_{HFE} = \dot{m}_{HFE} \cdot c_{p,HFE} \cdot \left(t_{HFE,out} - t_{HFE,in} \right) \tag{7.5}$$

The specific thermal capacity $c_{p,HFE}$ is that of pure HFE. It is a default function of temperature received from the manufacturer that is corrected for the purpose of calibration in Chapter 7.4.3. Equation 7.25 gives the corrected function for $c_{p,HFE}$. The inside surface area A_i for the micro-fin tubes is calculated from Equation 5.7. The HFE temperature difference between inlet and outlet of the test section is measured with two thermocouples and the mass flow is measured with the mass flow meter. According to Figure 7.4 the total heat flow into the HFE consists of following portions.

$$\dot{Q}_{HFE} = \dot{Q}_{CO2} + \dot{Q}_{amb,ts} + \dot{Q}_{con} \tag{7.6}$$

$\dot{Q}_{CO2}$ is the condensation heat flow from the CO_2 inside the test section. $\dot{Q}_{con}$ is the axial heat flow through the cross sectional area of the inner test section pipe. It is calculated in Chapter 7.4.2 and is given by Equation 7.14. $\dot{Q}_{amb}$ is the heat transmission from the environment through the insulation into the test section i.e. into the HFE steam. It is calculated in Chapter 7.4.3 and is given by Equation 7.26.

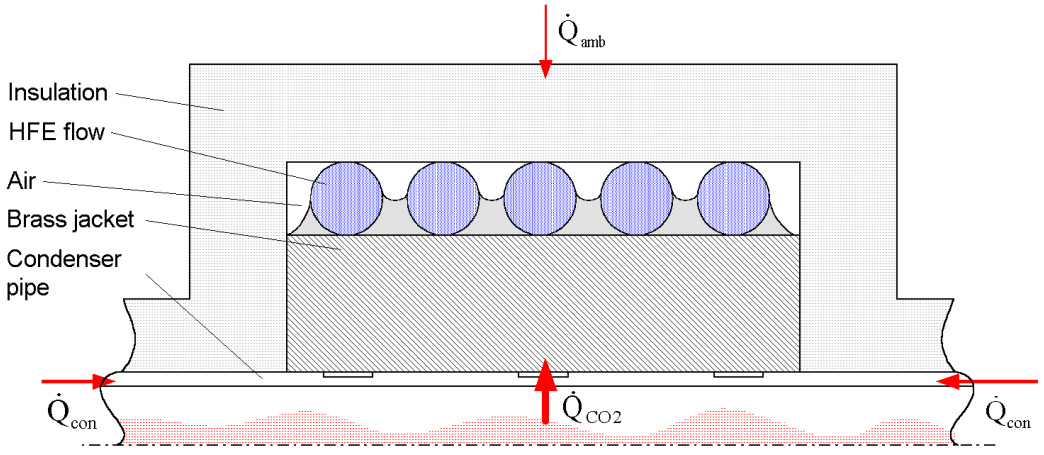

Figure 7.4: Heat components flowing into the HFE steam.

The heat transfer coefficient α_i is calculated only from $\dot{Q}_{CO2}$. The measured term $\dot{Q}_{HFE}$ must therefore be reduced by $\dot{Q}_{con}$ and $\dot{Q}_{amb}$. Combining Equation 7.4, 7.5 and 7.6 results in Equation 7.7.

$$\alpha_i = \left(\dot{Q}_{HFE} - \dot{Q}_{amb} - \dot{Q}_{con}\right) / \left(A_i \cdot \left(t_{sat} - t_{w,i,ts}\right)\right) \tag{7.7}$$

7.4.2 Correction of heat conduction

Before and after the test section the condensation of CO_2 to the cooled tube wall releases heat into the tube wall. That heat $\dot{Q}_{con}$ is conducted through the cross sectional area of the tube into the HFE flow. As the condenser test section consists of a single short pipe the radial transferred heat flow from the CO_2 is of a low amount. Hence the axial transferred heat through conduction is relatively high up to 25% compared to the radial transferred heat into the test section. Table 7.1 gives detailed information. It is therefore necessary to compensate for the heat conduction. Calculation of $\dot{Q}_{con}$ is done by a finite element code. The finite element code relies on five assumptions:

- Firstly the pipe element immediately following the test section is at the temperature of the average wall thermocouple reading.
- Secondly the pipe element far away from the test section is at the saturation temperature of the CO_2 shown in Figure 7.6.
- Another assumption is that the heat transfer coefficient of the CO_2 in the finite elements is the same as it was in the test section.
- The environmental heat transmission through the insulation of the finite element is neglected.
- Finally the conduction effect on the left side of the test section is assumed to be identical to that on the right side and the quality change in the test section is assumed to be negligible.

The code is applied to the section of pipe to the right of the test section. According to Figure 7.5 each element has three heat loads. $\varphi_{n,in1}$ is the heat input by conduction from the element on the right, $\varphi_{n,out}$ is the heat load conducted to the element on the left and $\varphi_{n,in2}$ is the heat load from the CO_2 inside the pipe. The element variable is n.

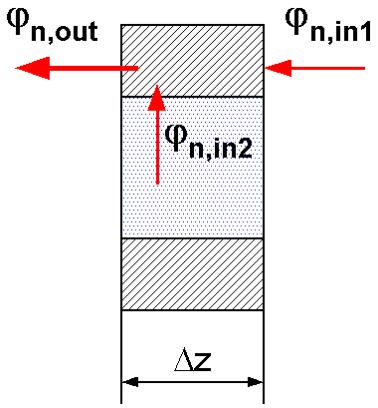

Figure 7.5: Finite Element with heat loads.

$$\varphi_{n,out} = \varphi_{n.in\,1} + \varphi_{n,in\,2} \tag{7.8}$$

$$\varphi_{n,in\,1} = k_{eff} / \Delta z \cdot A_{cs} \cdot \left(t_{n+1,w} - t_{n,w}\right) \tag{7.9}$$

$$\varphi_{n,in\,2} = \alpha_i \cdot A_{i,elt} \cdot \left(t_{sat} - t_{n,w}\right) \tag{7.10}$$

$$\varphi_{n,out} = k_{eff} / \Delta z \cdot A_{cs} \cdot \left(t_{n,w} - t_{n-1,w}\right) \tag{7.11}$$

Where Δz is the length and $A_{i,elt}$ is the inner surface of one element. For the smooth tube k_{eff} is the thermal conductivity of copper. As a micro-fin tube is soldered into an outer tube the effective total thermal conductivity k_{eff} has to be calculated from the cross sectional areas covered with copper and tin and the conductivities of the two materials.

$$k_{eff} = \left[1/\left(k_{Cu} \cdot A_{cs,Cu}\right) + 1/\left(k_{Sn} \cdot A_{cs,Sn}\right)\right]^{-1} / A_{cs} \tag{7.12}$$

Since the heat transfer coefficient α_i is dependent on the term $\dot{Q}_{con}$ and $\dot{Q}_{con}$ is dependent on α_i, the algorithm becomes iterative. Figure 7.6 shows the tube part left of the test section divided into finite elements and gives boundary conditions for the iteration.

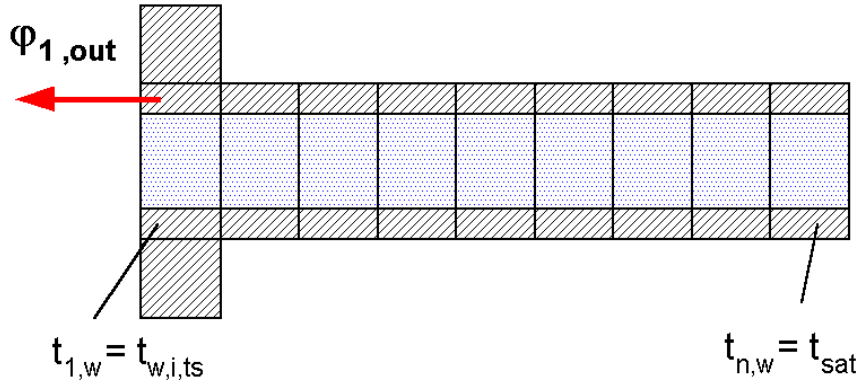

Figure 7.6: Pipe right of the test section divided into n finite elements, with boundary conditions.

$$\dot{Q}_{con} = 2 \cdot \varphi_{1,out} \tag{7.13}$$

$\varphi_{1,\,out}$ is the heat transferred into the test section by conduction of the first element that includes the heat loads from all other elements. The result is doubled to get the total heat in by conduction as this correction is necessary for both sides of the test section. $\dot{Q}_{con}$ can be approximated by Equation 7.14.

$$\dot{Q}_{con} = 2 \cdot k_{eff} / \sum \Delta z \cdot A_{cs} \cdot \left(t_{sat} - t_w\right) \tag{7.14}$$

Where total length of all finite elements is usually 10 cm. Table 7.1 shows values of $\dot{Q}_{con}$ at important measurement points.

7.4.3 Correction of heat transmission

The UA value represents the heat transfer coefficient multiplied with the heat transfer surface of the test sections. As the surface area and the heat transfer coefficient cannot be calculated or measured exactly both values are combined to the UA value.

$$\dot{Q}_{amb} = \alpha_{eff} \cdot A \cdot LMTD \tag{7.15}$$

$$\dot{Q}_{amb} = UA \cdot LMTD \tag{7.16}$$

Where LMTD is the logarithmic mean temperature difference. The purpose of the UA value is to compensate for the heat transmission from the environment into sections of the test rig where temperatures are measured to calculate enthalpies. These parts are the calorimeter, the condenser test section and the pipe connection calorimeter with the test section. UA values for each of the three sections are received from single phase experiments.

In order to calculate the UA value of the calorimeter UA_{cal}, subcooled CO_2 is pumped at a measured mass flow rate through the calorimeter and the thermocouples $t_{cal,i}$ and $t_{cal,o}$ record the inlet and outlet temperatures. The room temperature is recorded by an onboard thermistor in the data logger. The transferred $\dot{Q}_{amb}$ and the log mean temperature difference are then determined by the following equations:

$$\dot{Q}_{cal} = \dot{Q}_{el,cal} + \dot{Q}_{amb,cal} \tag{7.17}$$

$$\dot{Q}_{cal} = \dot{m}_{CO_2} \cdot c_{p,CO_2} \cdot \left(t_{cal,out} - t_{cal,in}\right) \tag{7.18}$$

$$LMTD_{UA,Cal} = \frac{\Delta t_{max} - \Delta t_{min}}{\ln\left(\Delta t_{max} / \Delta t_{min}\right)} = \frac{\left(t_{cal,i} - t_{room}\right) - \left(t_{cal,o} - t_{room}\right)}{\ln\left(\left(t_{cal,i} - t_{room}\right) / \left(t_{cal,o} - t_{room}\right)\right)} \tag{7.19}$$

Data was collected for three different CO_2 temperatures and a linear fit was applied to the results which gives UA_{cal} = 0.1923 $W \cdot K^{-1}$. The UA value for the length of pipe is calculated in a similar fashion. The results of the linear fit give UA_{pipe} = 0.1714 $W \cdot K^{-1}$.

The UA value for the test section was calculated in a different fashion since the relatively short test section length could not provide a measurable temperature difference between the inlet and outlet. The pipe prior and after the test section was temporarily removed and sealed with insulation. A cartridge heater produced by Watlow was placed inside the test section at three different simulated heat loads. LMTD is calculated using Equation 7.19 with temperatures from Figure 7.7 that shows a temperature profile in the test section. HFE was running at close to test conditions. Equation 7.20 and 7.21 show two energy balances for the HFE side of the condenser test section.

$$\dot{Q}_{HFE} = \dot{Q}_{heater} + UA_{ts} \cdot LMTD_{ts} \tag{7.20}$$

$$\dot{Q}_{HFE} = \dot{m}_{HFE} \cdot c_{p,HFE} \cdot \left(t_{HFE,out} - t_{HFE,in}\right) \tag{7.21}$$

Heat capacity for HFE is defined as a linear function according to manufacturer's data.

$$c_{p,HFE} = 0.002\ kJ \cdot kg^{-1} \cdot K^{-2} \cdot t_{HFE,m} + 1.133\ kJ \cdot kg^{-1} \cdot K^{-1} \tag{7.22}$$

The added 1.133 kJ·K^{-1} is then replaced by a correction factor $c_{p,HFE,c}$ to be able to create a linear function for the environmental heat flow to the test section $\dot{Q}_{amb,ts}$. Inserting Equation 7.20 and 7.22 into Equation 7.21 gives Equation 7.23 that can be rewritten to the form of a linear equation with a multiplying and an offset correction term.

$$\dot{m}_{HFE} \cdot \left(0.002\ \text{kJ} \cdot \text{kg}^{-1} \cdot \text{K}^{-2} \cdot t_{HFE,m} + c_{p,HFE,c}\right) \cdot \Delta t_{HFE} = W_{heater} + UA_{ts} \cdot LMTD_{ts} \tag{7.23}$$

$$\frac{W_{heater} - \dot{m}_{HFE} \cdot 0.002\ \text{kJ}^{-1} \cdot \text{Kg}^{-1} \cdot \text{K}^{-2} \cdot t_{HFE,m} \cdot \Delta t_{HFE}}{LMTD_{ts}} = \frac{\dot{m}_{HFE} \cdot \Delta t_{HFE}}{LMTD_{ts}} \cdot c_{p,HFE,c} - UA_{ts} \tag{7.24}$$

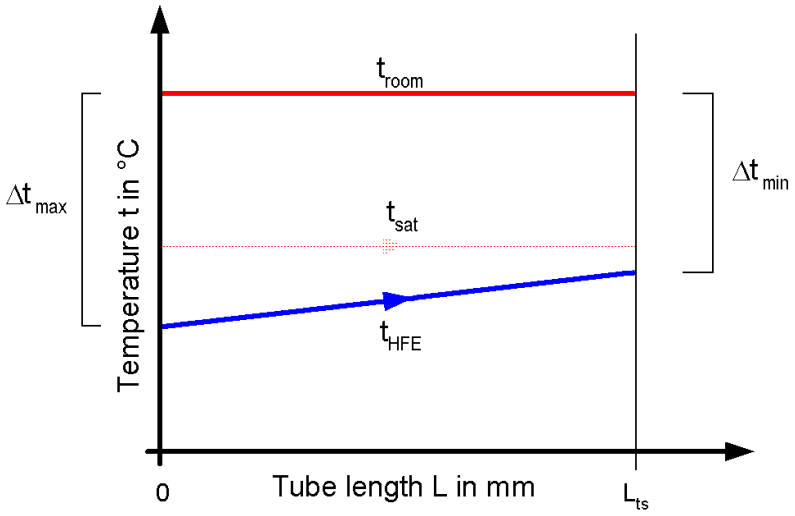

Figure 7.7: Temperature profile at the test section. Note that the test section operates similar to a cross flow heat exchanger.

Five separate calibration tests were run and a linear least square fit was applied, resulting in the correction factor $c_{p,HFE,c}$ = 1.232 kJ·kg^{-1}·K^{-1} and the term is UA_{ts} = 0.005061 W. Environmental heat $\dot{Q}_{amb,ts}$ and $\dot{Q}_{HFE}$ can then be calculated to.

$$c_{p,HFE} = c_{p,HFE,c} + 0.002\ \text{kJ} \cdot \text{kg}^{-1} \cdot \text{K}^{-1} \cdot \left(t_{HFE,out} + t_{HFE,in}\right)/2 \tag{7.25}$$

$$\dot{Q}_{amb,ts} = UA_{ts} \cdot \left[\frac{\left(t_{sat} - t_{HFE,o}\right) - \left(t_{sat} - t_{HFE,i}\right)}{\ln\left(\left(t_{sat} - t_{HFE,o}\right)/\left(t_{sat} - t_{HFE,i}\right)\right)}\right] \tag{7.26}$$

From the values in Table 7.1 it is obvious that the influence of $\dot{Q}_{amb,ts}$ is much less important than the influence of $\dot{Q}_{con}$ at critical measurement points. Measurement parameter at critical measurement points are given as t_{sat} in °C, G in kg m^{-2} s^{-1}, t_{sat} - t_w in K and quality x.

Table 7.1: Values for the heat flows $\dot{Q}_{con}$, $\dot{Q}_{amb,ts}$ relative to $\dot{Q}_{CO2}$.

t_{sat}/G/t_{sat} - t_w/x/	$\dot{Q}_{CO2}$	$\dot{Q}_{con}$	$\dot{Q}_{amb,ts}$	$\dot{Q}_{con}/\dot{Q}_{CO2}$	$\dot{Q}_{amb,ts}/\dot{Q}_{CO2}$
°C/kg·m^{-2}·s^{-1}/K/-/	W	W	W	%	%
-15/400/6/0,1	46.5	11.9	0.3	25.6	0.7
-15/400/3/0,1	29.7	7.4	0.3	24.9	1.0
-15/200/6/0,1	42.9	10.7	0.3	24.8	0.6
-15/200/30,1	23.1	5.5	0.2	23.7	1.0
-25/400/6/0,1	67.8	15.3	0.3	22.6	0.5
-25/400/3/0,1	24.9	5.9	0.3	23.7	1.2
25/200/6/0,1	41.9	10.6	0.3	25.3	0.8
-25/200/3/0,1	26.1	6.1	0.2	23.5	0.9

7.5 Calculation of quality

As the heat transfer coefficients are measured at definite local qualities it is necessary to calculate the quality at the inlet and outlet of the condenser test section. Subcooled CO_2 is provided by the pump and the enthalpy at the inlet of the calorimeter is calculated from the measured pressure and temperature. The enthalpy of the subcooled state at the inlet of the calorimeter is increased by the calorimeter heat and the environmental heat input into the calorimeter and the pipe to the test section given in Equation 7.27. From the enthalpy at the inlet of the test section the quality is calculated in Equation 7.28. During condensation quality decreases slightly. Enthalpy at the outlet of the test section is calculated by subtracting the heat flow $\dot{Q}_{CO2}$, that can be calculated from Equation 7.4, from the inlet enthalpy of CO_2 given in Equation 7.29. The mean vapor quality is calculated using the arithmetic mean value of outlet and inlet qualities given in Equation 7.30.

$$h_{ts,in} = h_{cal,in} + \left(\dot{Q}_{cal,el} + \dot{Q}_{amb,cal} + \dot{Q}_{amb,pipe}\right) / \dot{m}_{CO2} \tag{7.27}$$

$$x_{ts,in} = \left(h_{ts,in} - h'_{ts}\right) / \left(h''_{ts} - h'_{ts}\right) \tag{7.28}$$

$$x_{ts,out} = x_{ts,in} - \dot{Q}_{CO2} / \left(\dot{m}_{CO2} \cdot h_{lv}\right) \tag{7.29}$$

$$x_{ts,m} = \left(x_{ts,in} + x_{ts,out}\right) / 2 \tag{7.30}$$

8. Measurement Uncertainties

8.1 Basic statistics

According to Moffat [17] the uncertainty δR of a calculated result R can be estimated with the Taylor simplification of error propagation. The root-sum-square combination of the effects of the individual parameters gives the uncertainty of the result R.

$$\delta R = \sqrt{\left(\sum_{i=1}^{N} \frac{\partial R}{\partial X_i} \delta X_i \right)^2} \tag{8.1}$$

Here δX_i is the uncertainty in the variable X_i and the result R is calculated from a set of measurements and is therefore a function of measured variables X_i .

$$R = R(X_2, X_2, X_3, ..., X_N) \tag{8.2}$$

The partial derivative is the sensitive coefficient for the result R with respect to the measurement X_i. Each term in Equation 8.1 represents the contribution made by the uncertainty in one variable δX_i to the overall uncertainty in the result δR. This procedure is valid if three conditions are fulfilled.

- Each measurement is independent.
- Repeated observations would display a Gaussian distribution.
- The uncertainty in each measurement was initially expressed with the same confidence.

All uncertainty data are based on a confidence level of 95%.

8.2 Uncertainty in measured parameters

Measured parameters are temperature differences, mass flow, absolute and differential pressure and electrical power input.

Uncertainty for temperature reading is δt = 0.1 K for calibrated thermocouples relative to each other. Most important measurements at the test section are the inlet and outlet temperatures of the HFE flow. From this temperature difference the heat flow and the heat transfer coefficient are calculated. At the test section twelve thermocouples measure the mean temperature. Calibration was done by using the setup of the test rig including cables, datalogger and reference temperature. The uncertainties of these instruments are therefore included in the uncertainty of the thermocouples.

Mass flow is measured with Coriolis mass flow meters for both refrigerant and coolant (HFE) mass flow. Uncertainty of these meters is almost constant at 0.15% of the reading for mass flow rates above 4% of full scale. At highest mass flows for CO_2 of $\dot{m}_{CO2}$ = 11.7 g·s^{-1} uncertainty is $\delta\dot{m}_{CO2}$ = 0.018 g·s^{-1}.

Uncertainty in absolute pressure measurement is δp = 0.1% of the pressure reading which results in a maximum uncertainty at the highest pressure reading at a saturation temperature of t_{sat} = -15 °C of δp = 0.02 bar.

The uncertainty in the output value of the electrical power transducer is given as 0.2% of the measured value. The maximum power for heating is 2 kW for the refrigerant preheater and 2 kW for the HFE heater which gives maximum uncertainties of $\delta\dot{Q}_{el}$ = 4 W.

8.3 Uncertainty in heat transfer coefficient

Error propagation is calculated with the Taylor simplification equation. The final error in heat transfer coefficients consists of partial deviations of the complete equation for the HTC multiplied by uncertainty values of each measured variable. Important deviations are listed below.

$$\delta\alpha_i = \left[\left(\frac{\partial \alpha_i}{\partial \dot{m}_{HFE}} \cdot \delta \dot{m}_{HFE} \right)^2 + \left(\frac{\partial \alpha_i}{\partial c_{p,HFE,b}} \cdot \delta c_{p,HFE,b} \right)^2 + \left(\frac{\partial \alpha_i}{\partial UA_{ts}} \cdot \delta UA_{ts} \right)^2 + \left(\frac{\partial \alpha_i}{\partial t_{HFE,i}} \cdot \delta t_{HFE,i} \right)^2 + \left(\frac{\partial \alpha_i}{\partial t_{HFE,o}} \cdot \delta t_{HFE,o} \right)^2 + \left(\frac{\partial \alpha_i}{\partial t_{ref}} \cdot \delta t_{ref} \right)^2 + \left(\frac{\partial \alpha_i}{\partial t_w} \cdot \delta t_w \right)^2 + \left(\frac{\partial \alpha_i}{\partial p_{CO2}} \cdot \delta p_{CO2} \right)^2 + \left(\frac{\partial \alpha_i}{\partial k_{eff}} \cdot \delta k_{eff} \right)^2 \right]^{0.5} \quad (8.3)$$

The sensitive coefficients are too extensive to be listed here. They were programmed to calculate uncertainties for every data point. Error calculation is double checked by EES internal error propagation that gives comparable results for error in heat transfer coefficients. Errors for HTCs range from 8% to 15% of measured values. In general the error in HTC is high due to the short test section and the low transferred heat $\dot{Q}_{CO2}$.

Table 8.1 shows the influence of individual uncertainties on the total uncertainty in heat transfer coefficient at a representative measurement point. The percentage of error is calculated from Equation 8.4.

$$\delta R_i / \delta R = \frac{\left(\delta\alpha_i / \partial X_i \cdot \partial X_i \right)^2}{\delta \alpha_i^2} \cdot 100 \quad (8.4)$$

Table 8.1: Absolute and relative uncertainty at measurement parameters of t_{sat} = -15 °C, G = 400 kg·m^{-2}·s^{-1}, t_{sat} – t_w = 6 K, x = 0.5

Measured parameter	Symbol	Accuracy	Unit	$\delta R_i/\delta R$ in %
HFE massflow	$\dot{m}_{HFE}$	0,00005	kg·s^{-1}	0.07
HFE cp offset	$c_{p,HFE,c}$	0,03700	kJ·kg^{-1}·K^{-1}	32.34
UA test section	UA_{ts}	0,03560	W·K^{-1}	6.97
HFE inlet temperature	$t_{HFE,in}$	0,10000	K	27.27
HFE outlet temperature	$t_{HFE,out}$	0,10000	K	26.95
Reference temperature	t_{ref}	0,10000	K	0.00
Wall temperature	t_w	0,02887	K	1.03
Saturation pressure	p_{sat}	4,57500	kPa	5.29
Conductivity of tube	k_{eff}	1,18500	W·m^{-1}·K^{-1}	0.08

8.4 Uncertainty in quality

Mean quality is calculated from the inlet and outlet quality at the test section. To calculate quality at the outlet of the test section all heat flows have to be taken into account. Using the same Taylor simplification as for the uncertainty calculation of HTCs would result in even more complex deviations as the HTC is a variable in the

function to calculate the outlet quality after the test section. As a comparison between the calculated uncertainty of HTC and the EES's program integrated uncertainty estimation proved the applicability of the program routine it can be used for other uncertainty calculations. Uncertainty of quality shown as error bars in Chapter 9 is the change in quality in the test section. As the condenser test section is a short pipe of 15 cm length the change of quality in the test section is low and the error in quality is small.

9. Results and discussion

Experimental data for heat transfer coefficient and pressure drop are available at saturation temperatures of t_{sat} = -25 °C and t_{sat} = -15 °C. Mass fluxes are G = 200 kg·m^{-2}·s^{-1}, G = 300 kg·m^{-2}·s^{-1} and G = 400 kg·m^{-2}·s^{-1}. Results for the smooth tube are shown in Chapter 9.1 and 9.2, results for the micro-fin tube are shown in Chapter 9.3 and 9.4. Comparisons of smooth and micro-fin tube are made in Chapter 9.5.

9.1 Heat transfer coefficient of CO_2 inside smooth tube

9.1.1 Effect of operating parameters

Important operating parameters are quality, temperature difference during condensation, mass flux and saturation temperature. Figure 9.1 shows heat transfer coefficients of CO_2 at saturation temperature t_{sat} = -15 °C. In general heat transfer coefficients increase from low to high qualities as the volume flow and the flow velocity increase. At higher mass flux this gradient is higher.

Temperature differences between saturation temperature of the CO_2 and the inner wall temperature are Δt = 3 K and Δt = 6 K. The smallest error bars for HTCs and quality are the error bars for t_{sat} = -15 °C and Δt = 3 K. The error bars show that the effect of increased temperature difference during condensation is negligible compared to the error in HTC. In further figures for the smooth tube heat transfer coefficients will be regarded as independent of temperature difference. Note that for quality x = 0.1 HTCs for Δt = 3 K are 5% higher than HTCs for Δt = 6 K. As the error in heat transfer coefficient is smaller for data points with Δt = 3 K, these data will be preferred in the presentation.

HTCs for higher mass flux are higher than HTCs for low mass flux. Only for quality x = 0.1 HTCs are not strongly dependent on mass flux. From Figure 9.2 it can be seen, with respect to the error bars, that the HTCs are a linear function of the mass flux. When the mass flux is doubled HTCs increase by 60% at quality x = 0.5.

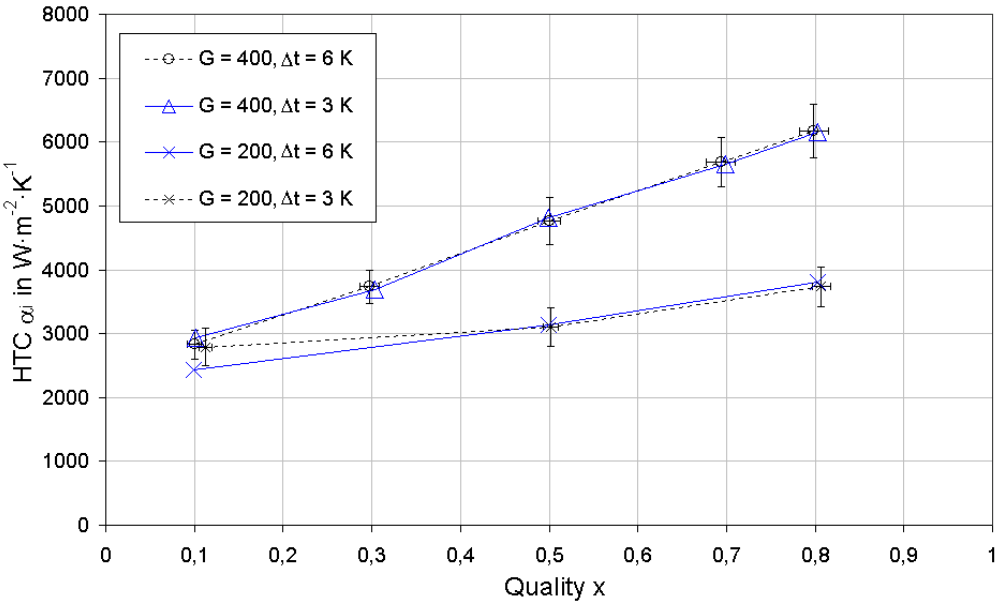

Figure 9.1: Heat transfer coefficient of CO_2 inside smooth tube at varying quality x and at t_{sat} = -15 °C. Note that $\Delta t = t_{sat} - t_{w,i}$ and G is in kg·m^{-2}·s^{-1}.

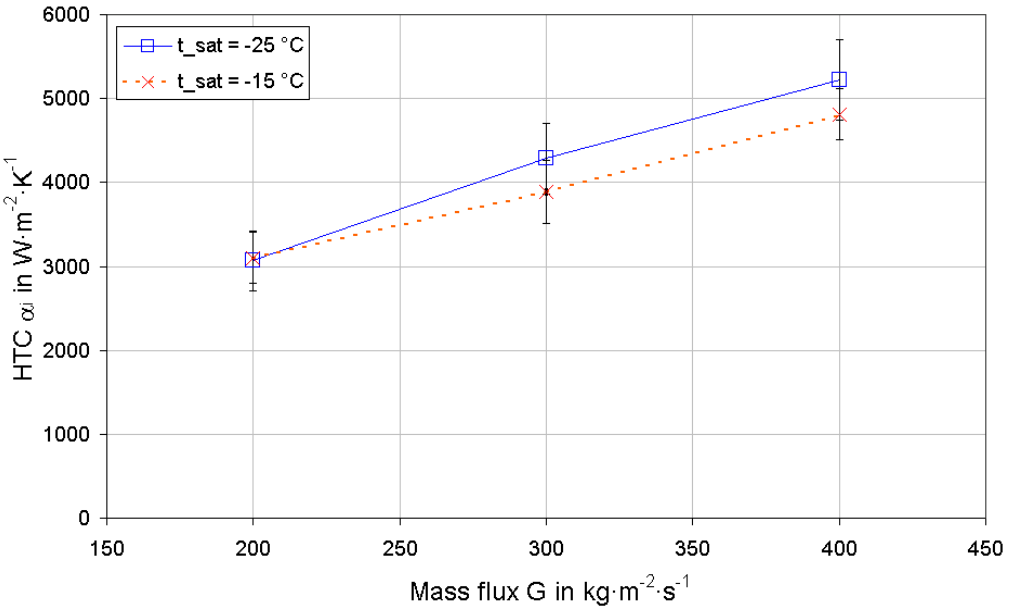

Figure 9.2: Heat transfer coefficient of CO_2 inside smooth tube at quality x = 0.5, varying mass flux and saturation temperatures.

Figure 9.3 shows heat transfer coefficients of CO_2 at mass fluxes of G = 200 $kg \cdot m^{-2} \cdot s^{-1}$, G = 300 $kg \cdot m^{-2} \cdot s^{-1}$ and G = 400 $kg \cdot m^{-2} \cdot s^{-1}$ and at saturation temperatures t_{sat} = -15 °C and t_{sat} = -25 °C. HTCs are higher at lower saturation temperature and lower saturation pressure. This is according to the experimental data for R-22 given in Chapter 7.1. The decrease of saturation temperature by 10 K decreases the density of the gas phase by 40% which increases the ratio of liquid and vapor densities. Void fractions are given by Cavallini, Nonzu and Yu and Koyama. At t_{sat} = -25 °C and quality x = 0.1 the void fraction is low and ranges from $\varepsilon_{0.1,Nonzu}$ = 0.1 and $\varepsilon_{0.1,\ Cavallini}$ = 0.4 to $\varepsilon_{0.1,\ Yu}$ = 0.5. At low void fraction this density ratio may be less relevant for the HTCs explaining that at low quality there is little difference between HTCs for high and low saturation temperatures. At higher qualities, void fractions range from $\varepsilon_{0.8,Nonzu}$ = 0.7 and $\varepsilon_{0.8,\ Cavallini}$ = 0.8 to $\varepsilon_{0.7,\ Yu}$ = 0.9 and the gravitational effect on the liquid phase due to it's higher density compared to the vapor phase may be more important. An additional positive effect of the density decrease of the gas phase at lower temperatures is the increase in the volume flow and flow velocity which increases HTCs.

Another important factor to describe the effect of saturation temperature is the dynamic viscosity. This viscosity is 16% higher at lower saturation temperature, which is the increase in HTCs for lower saturation temperature at quality x = 0.8 and high mass flux.

The surface tension is also important for heat transfer coefficients. The decrease of saturation temperature by 10 K increases surface tension by 30%. Surface tension can be regarded as work per surface area of a liquid droplet and higher surface tension may increase HTCs. More energy from the condensation process can be stored as surface energy, which increases the condensation rate. This effect would also explain higher HTCs at quality x = 0.1 and lower saturation temperature, assuming the increased surface tension dries the upper tube wall and the vapor phase can condensate directly to the tube wall. On the other side the effect of condensation heat being stored as

surface energy would decrease the measured heat flow to the HFE thus decreasing measured HTCs. In addition the surface energy would be released again when the droplets combine at the end of the condensation process.

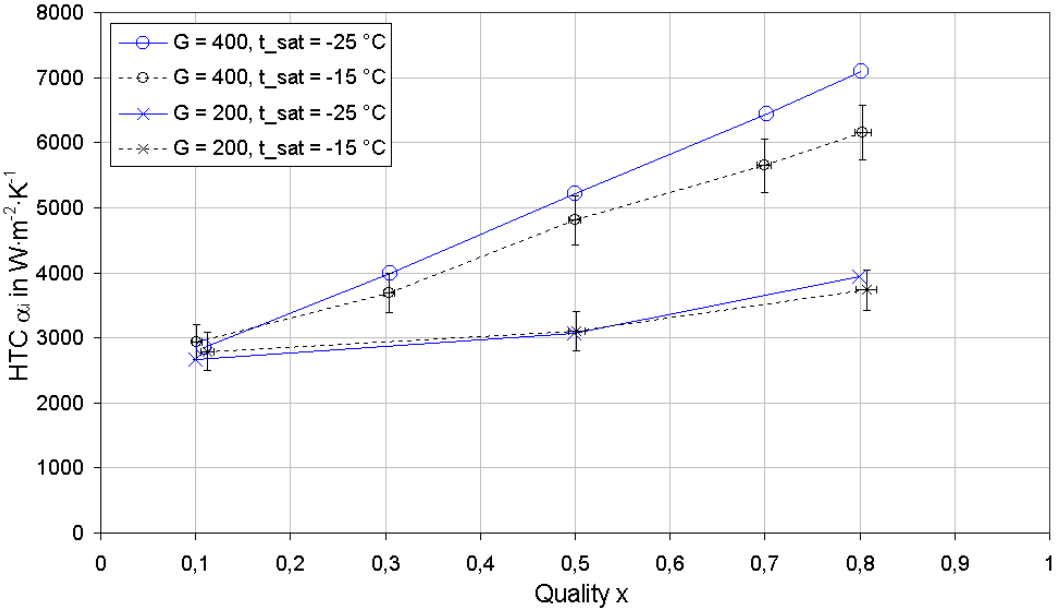

Figure 9.3: Heat transfer coefficient of CO_2 inside smooth tube at varying quality x and saturation temperatures. Note that G is in $kg \cdot m^{-2} \cdot s^{-1}$.

9.1.2 Comparison with correlations

Figure 9.4 shows heat transfer coefficients for condensation of CO_2 in smooth tubes. Experimental HTCs are compared to correlations by Dobson, Cavallini-Zecchin and Shah that were developed for conventional refrigerants like R-22 and explained in Chapter 5. Other correlations give comparable predictions of the CO_2 data but are not applied often. The experimental data for R-22 given in Figures 7.1 and 7.2 show over prediction by the correlations but good correspondence concerning the trend with increasing quality. For CO_2 the correlations predict much higher HTCs and the predicted trend is steeper than the trend of measured HTCs with increasing quality. In further data analysis it was found that the correlations for G = 200 $kg \cdot m^{-2} \cdot s^{-1}$ predict measured HTCs for G = 400 $kg \cdot m^{-2} \cdot s^{-1}$.

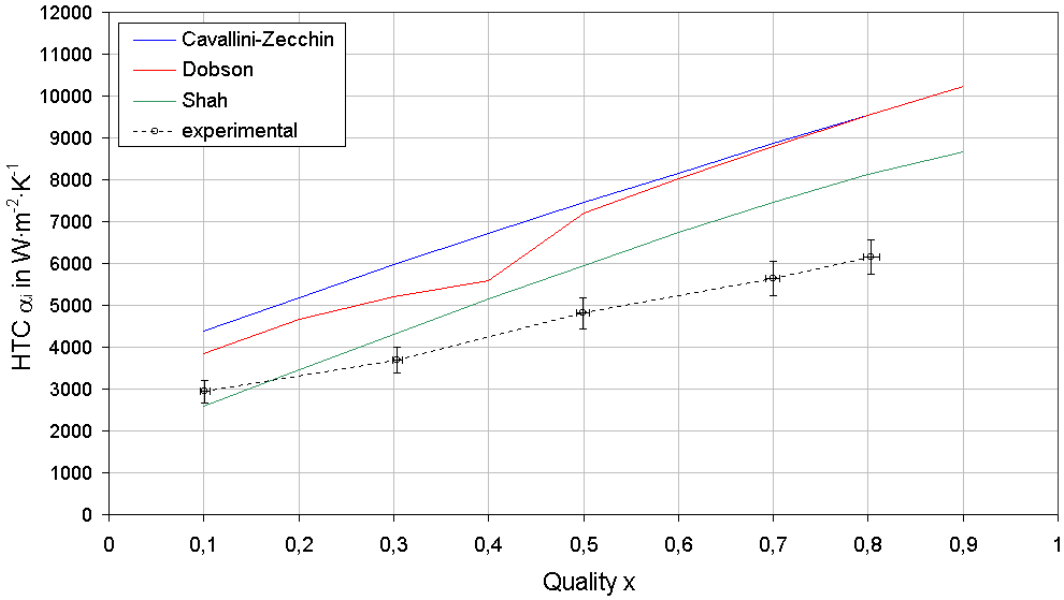

Figure 9.4: Comparison of heat transfer coefficient with correlations at varying quality x and t_{sat} = -15 °C and G = 400 kg·m^{-2}·s^{-1}.

9.2 Pressure drop inside smooth tube

Figure 9.5 shows pressure drop data for CO_2 inside the horizontal, adiabatic and smooth tube. Operating parameters are the saturation temperature of t_{sat} = -25 °C and varying mass fluxes. Pressure drop is predicted by the empirical correlation Equation 4.14. Experimental data follows the trend for high mass flux and is close to the predicted pressure drop at low mass flux. As the fluid velocity increases with increasing quality the frictional pressure drop increases proportionally. When an annular flow regime is established at medium qualities, additional friction is caused by wave generation at the upper tube and the increase of Δp_{ho} is higher. At high qualities the linear increase in horizontal pressure drop is reduced to a parabolic behavior. With increasing vapor fraction the liquid phase gets entrained and the annular liquid film disappears. The portion of friction caused by wave generation vanishes and the increase in total friction is reduced. At low mass flux the annular flow regime may not appear and the increase of Δp_{ho} with increasing quality is constant for all qualities.

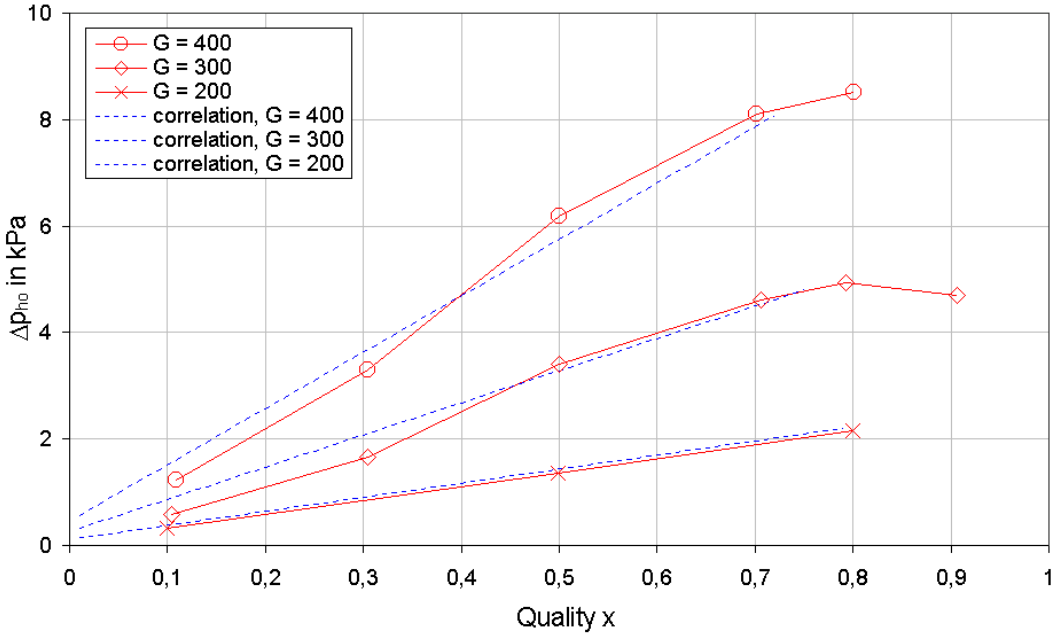

Figure 9.5: Adiabatic pressure drop of CO_2 inside smooth horizontal tube at varying quality x and mass fluxes and at t_{sat} = -25 °C. The empirical correlation given by Equation 4.14 is compared to experimental data. Note that G is in $kg \cdot m^{-2} \cdot s^{-1}$.

Figure 9.6 shows pressure drop data for CO_2 inside the vertical, adiabatic and smooth tube. Vertical pressure drop is caused by friction and the weight of the liquid column. For low qualities when most of the CO_2 mass flux is liquid, the fluid velocity is low and the gravitational effect is most important. At quality x = 0.1 the pressure drop due to an increase of altitude of 1 m which is the test section height can be calculated. Depending on the chosen void fraction the gravitational pressure drop is about Δp_g = 3 kPa. This explains the fact that both pressure drop for low and high mass fluxes are close to Δp_{ve} = 4 kPa. As the quality increases the frictional pressure drop for high mass flux increases stronger than the gravitational pressure drop decreases and the total pressure drop increases for high mass flux. At low mass flux the frictional term is less important and as the gravitational term decreases the total pressure drop for vertical flow decreases. Experimental data for t_{sat} = -15 °C show that for higher saturation temperature the vapor density is higher resulting in lower fluid velocity and lower frictional pressure drop both at low and high mass flux.

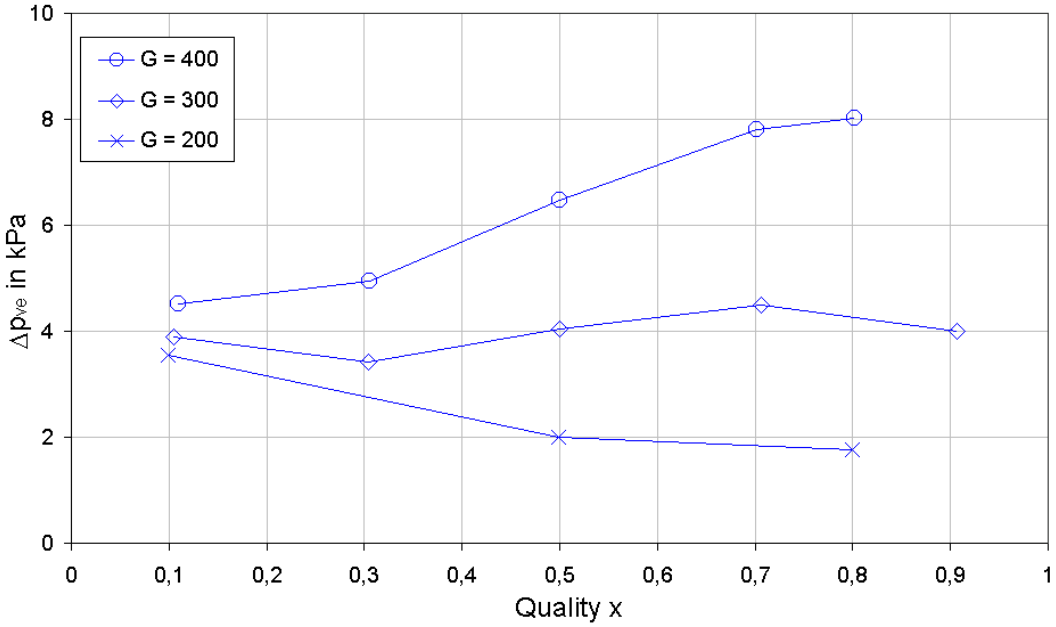

Figure 9.6: Adiabatic pressure drop of CO_2 inside smooth vertical tube at varying quality x, t_{sat} = -25 °C and different mass fluxes. Note that G is in $kg \cdot m^{-2} \cdot s^{-1}$.

9.3 Heat transfer coefficient of CO_2 inside micro-fin tube

9.3.1 Effect of operating parameters

Similar to Figure 9.1, Figure 9.7 shows HTCs measured at temperature differences between saturation and wall temperature of Δt = 3 K and Δt = 6 K. The error bars cover the difference in HTCs at different temperatures. Like HTCs inside the smooth tube, HTCs for the micro-fin tube are independent of the temperature difference during condensation. According to theory HTCs for higher temperature difference can be lower compared to HTCs at lower temperature difference. This behavior that can be observed at smooth tubes may result from a thicker condensate film that can only come into existence at low flow velocities. As the condensation rate is higher for Δt = 6 K, this condensate layer would be thicker and the total thermal resistance would be increased resulting in lower HTCs.

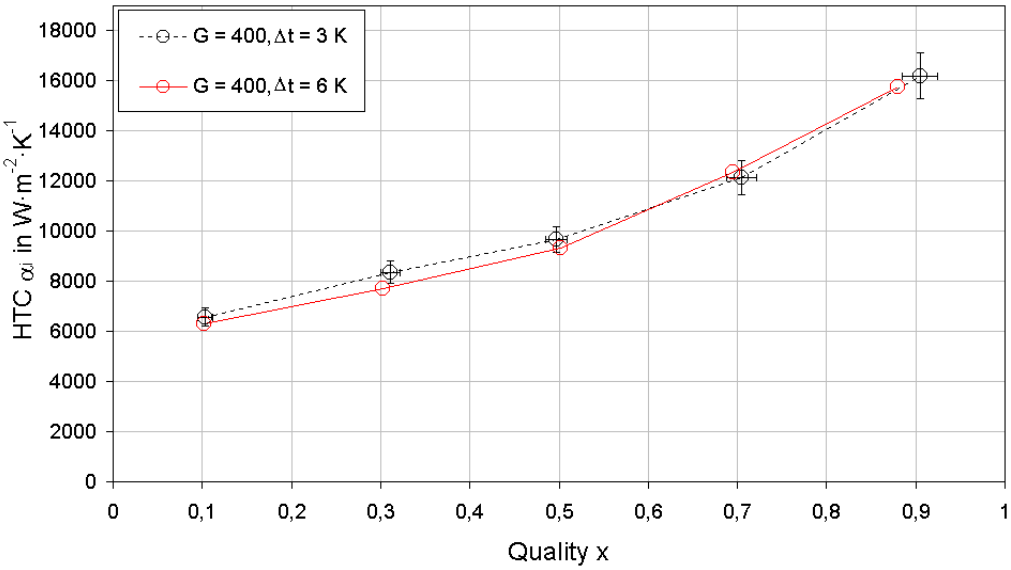

Figure 9.7: Heat transfer coefficient of CO_2 inside micro-fin tube at varying quality x at t_{sat} =-15 °C and varying temperature differences. Note that $\Delta t = t_{sat} - t_{w,i}$ and G is in $kg \cdot m^{-2} \cdot s^{-1}$.

One important difference between micro-fin and smooth tube is the effect of mass flux. Figure 9.8 shows that unlike HTCs for the smooth tube, HTCs for the micro-fin tube are not highly dependent on the mass flux. For most qualities, HTCs measured at 100% higher mass flux are only 10% higher. One possible explanation could be that fact that the turbulence caused by the higher flow rate is negligible compared to the turbulence caused by the micro-fins. Earlier studies have already shown that for higher pressures heat transfer coefficients for micro-fin tubes are much less dependent on mass flux as HTC for smooth tubes.

Figure 9.9 shows HTCs at saturation temperatures of t_{sat} = -25 °C and t_{sat} = -15 °C. HTCs are consistently higher for lower saturation temperature. Possible explanations for this behavior are given in Chapter 9.1.1. A comparison of Figure 9.1 and 9.9 shows that the increase in HTCs at lower saturation temperature at flux at G = 200 $kg \cdot m^{-2} \cdot s^{-1}$ for micro-fin tubes is stronger than for the smooth tubes. At G = 400 $kg \cdot m^{-2} \cdot s^{-1}$ the increase in HTC at lower temperature is of comparable relative amount. For the micro-fin tubes both HTCs for high and low mass fluxes are increased at lower saturation temperatures compared to the smooth tubes where the low mass fluxes were not influenced by changes in saturation temperature.

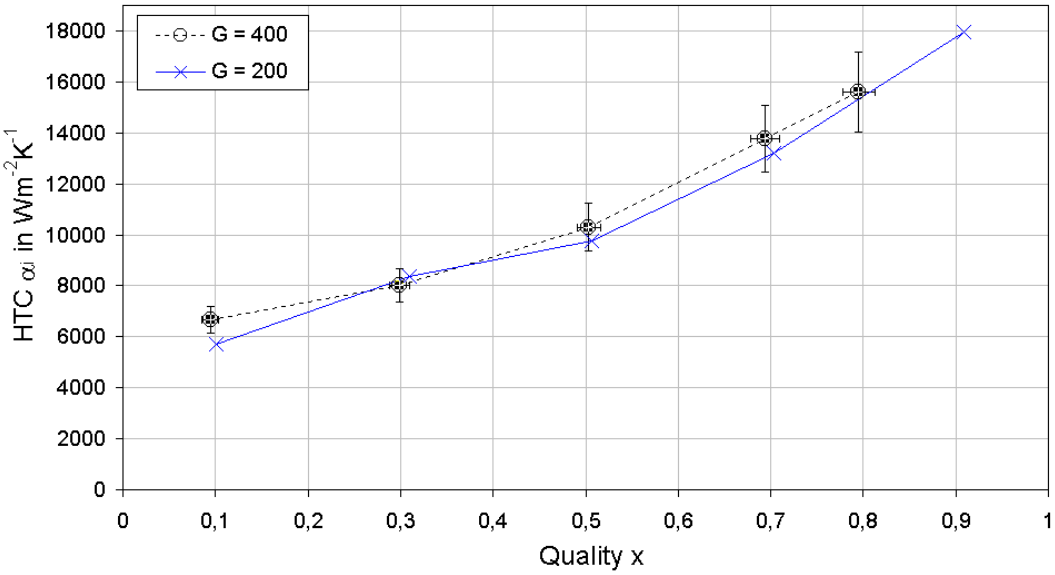

Figure 9.8: Heat transfer coefficient of CO_2 inside micro-fin tube at varying quality x at t_{sat} = -25 °C and varying mass fluxes. Note that G is in $kg \cdot m^{-2} \cdot s^{-1}$.

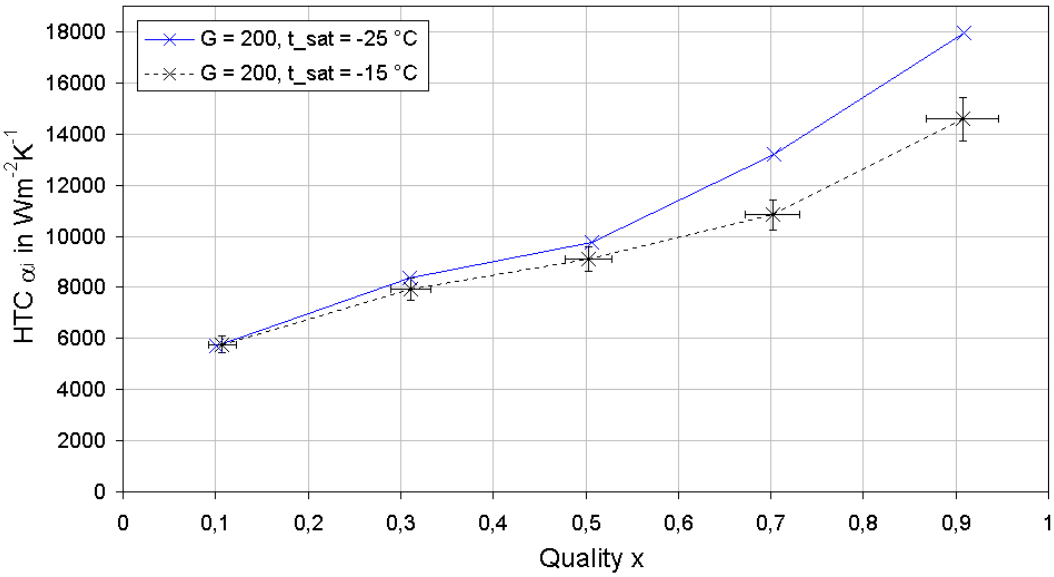

Figure 9.9: Heat transfer coefficient of CO_2 inside micro-fin tube at varying quality x and saturation temperatures. Note that G is in $kg \cdot m^{-2} \cdot s^{-1}$.

9.3.2 Comparison with correlations

Only Cavallini's correlation predicts heat transfer coefficients for CO_2 in micro-fin tubes in a 50% range of the measured HTCs at low mass flux. Other correlations predict much lower or higher HTCs. According to theory, Cavallini's correlation is independent of the temperature difference during condensation. Figure 9.10 shows predicted HTCs at t_{sat} = -25 °C and Figure 9.11 shows predicted HTCs at t_{sat} = -15 °C. At higher saturation temperature higher HTCs are predicted but the measured data show higher HTCs at lower saturation temperature. A comparison of Figure 9.10 and 9.11 shows that the correlation for t_{sat} = -25 °C is closer to the measured HTCs than at t_{sat} = -15 °C. Similar to the comparison of correlations with measured data for the smooth tube shown in Figure

9.4, measured HTCs for the enhanced tube are lower than predicted data. Over prediction of the smooth tube data is even higher than for the micro-fin tube. Also the heat transfer coefficients for R-22 are overpredicted. Again the correlation at low mass flux predicts the measured HTCs at high mass flux. The most important flaw of the Cavallini correlation is the fact that the predicted heat transfer coefficient is strongly dependent on the mass flux whereas the measurement results are rather independent of mass flux.

One explanation for the inaccurate prediction by the Cavallini correlation is the required boundary condition for the Prandel number which describes the ratio of momentum diffusivity to heat diffusivity. The correlation is applied out of its range as the required minimum Prandel number is not reached by CO_2 at low temperatures. A comparison of the Cavallini correlation applied for CO_2 and R-22 shows that the equivalent Reynolds number, which is calculated from the density ratio of liquid and vapor, is 30% lower for CO_2 than for R-22. Modifying this equivalent number could adjust Cavallini's correlation to the measured CO_2 data.

In addition the comparison of Figure 9.10 and 9.11 shows that the difference between high and low mass flux gets smaller at lower saturation temperature.

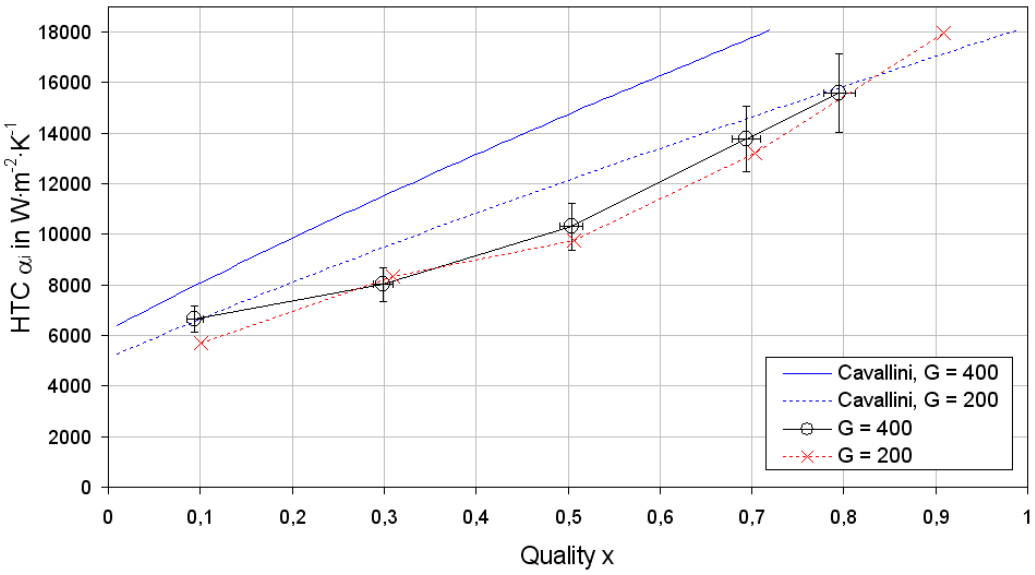

Figure 9.10: Comparison of heat transfer coefficient at varying quality x and different mass fluxes with the Cavallini correlation. Saturation temperature is t_{sat} = -25 °C. Note that G is in $kg \cdot m^{-2} \cdot s^{-1}$.

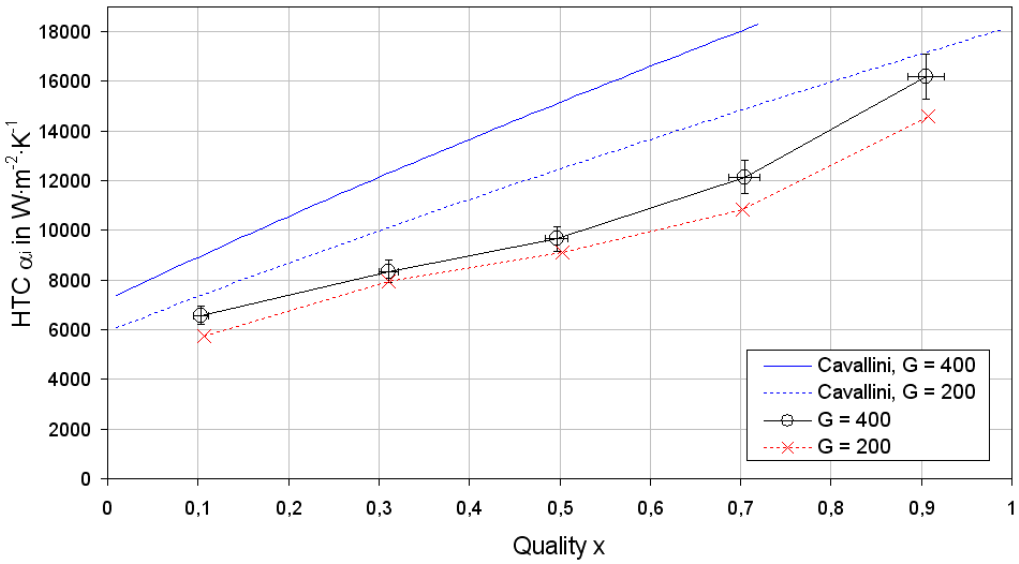

Figure 9.11: Comparison of heat transfer coefficient at varying quality x and different mass fluxes with the Cavallini correlation. Saturation temperature is t_{sat} = -15 °C. Note that G is in kg·m^{-2}·s^{-1}.

9.4 Pressure drop inside micro-fin tube

Figure 9.12 shows pressure drop date for CO_2 flowing in the horizontal adiabatic micro-fin tube. At lower saturation temperatures the horizontal pressure drop is higher than at higher saturation temperatures. This effect is stronger at higher mass flux. At lower saturation temperature the increase in horizontal pressure drop with increasing quality is higher. This effect could result from the lower vapor density at lower saturation temperature and subsequently lower fluid velocities. The decrease in vapor density by 40% results in an increase of frictional pressure drop of 40%. At high qualities when the heat transfer coefficient is highest, the pressure drop inside the horizontal tube is highest too especially at high mass flux. At low mass flux that results in slightly lower heat transfer coefficients than the high mass flux, the pressure drop inside the horizontal tube is strongly reduced.

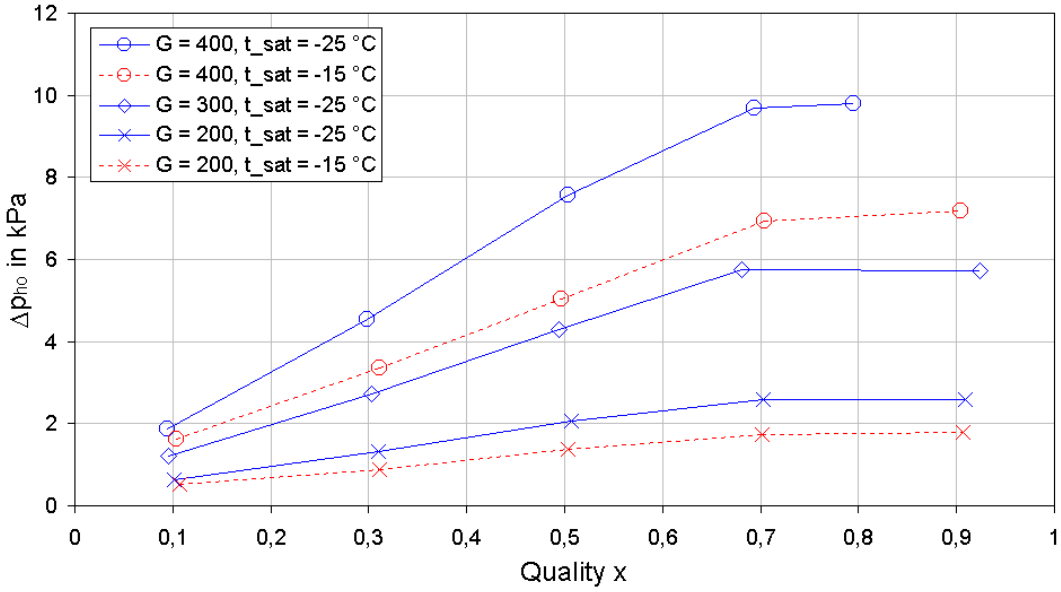

Figure 9.12: Measured pressure drop inside horizontal micro-fin tube at varying quality x, mass fluxes and saturation temperatures. Note that G is in $kg \cdot m^{-2} \cdot s^{-1}$.

Figure 9.13 shows measured pressure drop data for adiabatic, vertical flow. Similar to the pressure drop inside a horizontal tube, the pressure drop inside the vertical tube is higher at lower saturation temperatures. The increase due to lower saturation temperatures is equal in vertical pressure drop and in horizontal pressure drop. Similar to the vertical smooth tube the pressure drop inside the micro-fin tube increases with increasing quality for the high mass flux. For the low mass flux the pressure drop decreases with increasing quality. When the pressure drop of vertical flow is compared to the heat transfer coefficient, it is obvious that at high qualities and low mass flux highest heat transfer coefficients are reached with lowest pressure drops.

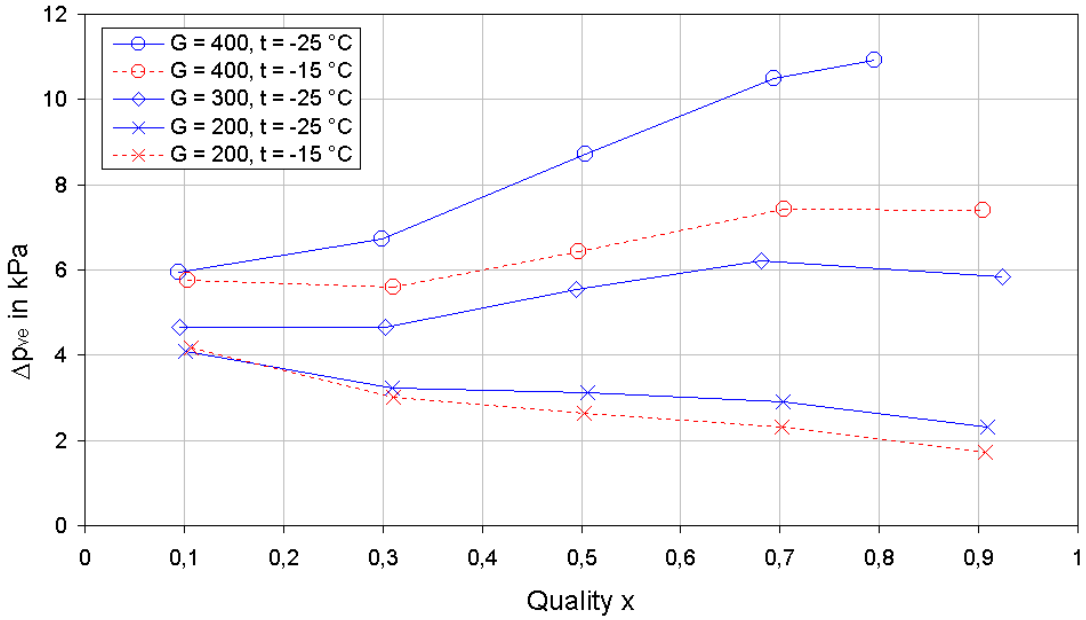

Figure 9.13: Measured pressure drop data inside vertical micro-fin tube at varying quality x, mass fluxes and saturation temperatures. Note that G is in $kg \cdot m^{-2} \cdot s^{-1}$.

9.5 Comparison of smooth and micro-fin tube

This chapter compares data for the micro-fin tube with data for the smooth tube. The micro-fin tube has a meltdown diameter of D_m = 6.26 mm compared to the inner diameter of the smooth tube D_i = 6.1 mm. A comparison is possible as the difference in diameter is smaller than the error in diameter measurement. For a micro-fin tube with a meltdown diameter of D_m = 6.1 mm the inner heat transfer coefficient and pressure drop would be insignificantly higher.

9.5.1 Comparison of heat transfer coefficient

Figure 9.14 shows heat transfer coefficients for the smooth and the micro-fin tube at the saturation temperature of t_{sat} = -15 °C and mass fluxes of G = 400 kg·m^{-2}·s^{-1} and G = 200 kg·m^{-2}·s^{-1}. As the HTCs for the micro-fin tube are only slightly dependent on mass flux, the increase of HTCs in the micro-fin tube compared to the smooth tube at low mass flux is higher than at high mass flux. This behavior is according to results of previous studies. The micro-fin structure may have a turbulence increasing effect that is independent on mass flux and is therefore more important at low mass flux when the flow is laminar.

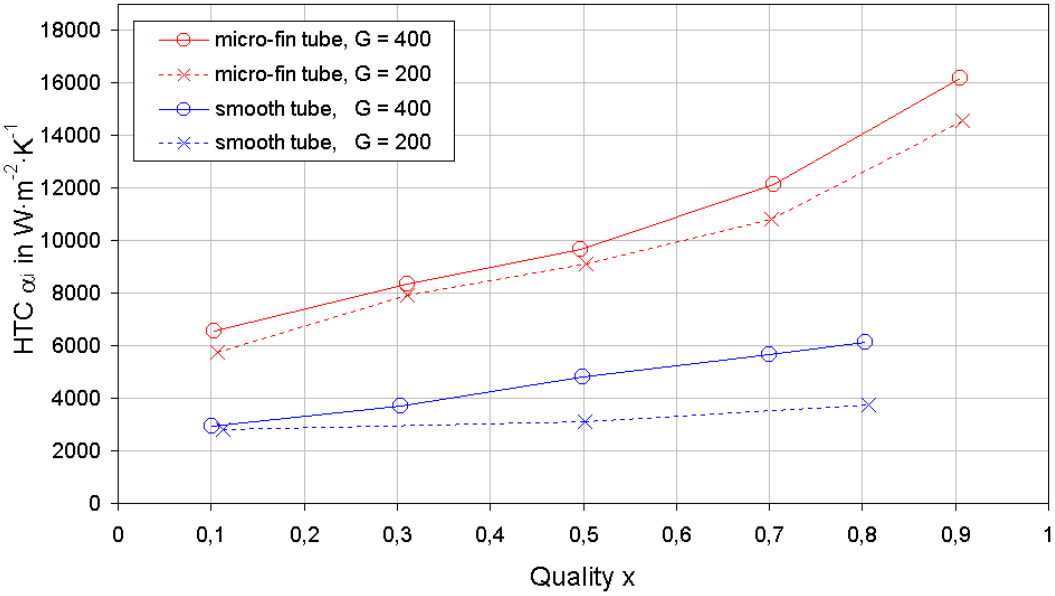

Figure 9.14: Comparison of heat transfer coefficient of CO_2 inside horizontal smooth and micro-fin tube at t_{sat} = -15 °C and different mass fluxes. Note that G is in kg·m^{-2}·s^{-1}.

A comparison of Figure 9.14 and 9.15 shows that lower saturation temperatures result in higher heat transfer coefficients especially at high mass flux and quality. The enhancement of heat transfer coefficients by the micro-fin tube is only slightly dependent on the saturation temperature.

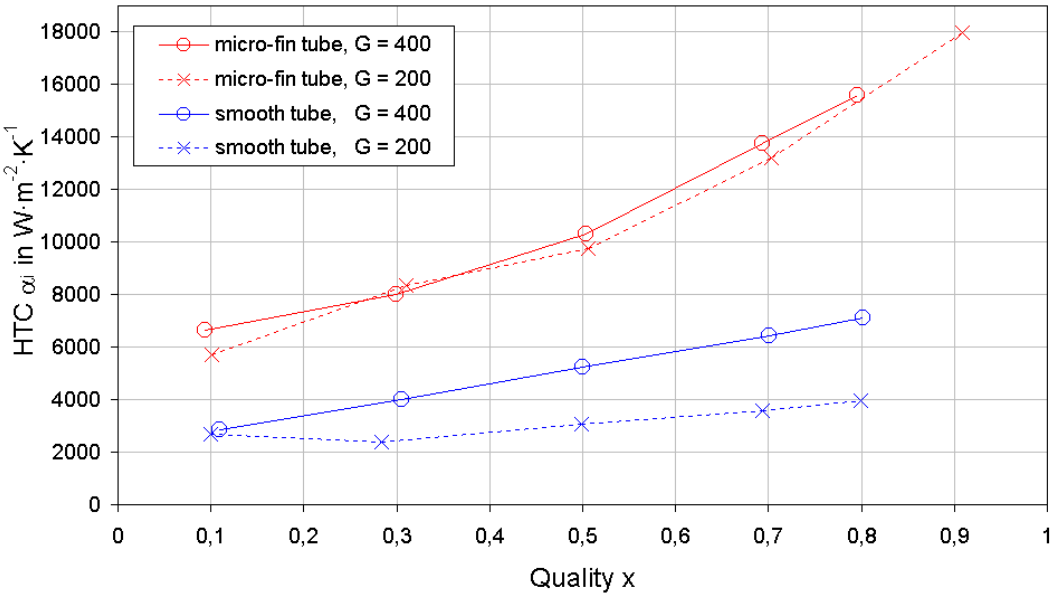

Figure 9.15: Comparison of heat transfer coefficient of CO_2 inside horizontal smooth and micro-fin tube at t_{sat} = -25 °C and different mass fluxes. Note that G is in $kg \cdot m^{-2} \cdot s^{-1}$.

Micro-fin tubes are characterized by higher inner surface area at the same inner diameter. For the micro-fin tube used in this study the increase in inner surface area compared to a smooth tube with the same meltdown diameter is 54%. The triangles in Figure 9.16 and 9.17 show HTCs of a smooth tube with the same inner surface area than the micro-fin tube. There is an additional increase of HTCs when the increase due to the increased surface area is compensated for. The increase in heat transfer due to the surface area increase is less than 20% of the total increase for low mass fluxes, but 50% of the increase for high mass fluxes. Possible explanations for this additional enhancement are the increased turbulence of the two phase flow, changes in flow patter and reduced thickness of the condensate film. A comparison of Figure 5.3 shows that the measured results are according to earlier experimental research. For low mass flux the enhancement of heat transfer coefficient by using the micro-fin tube is highest.

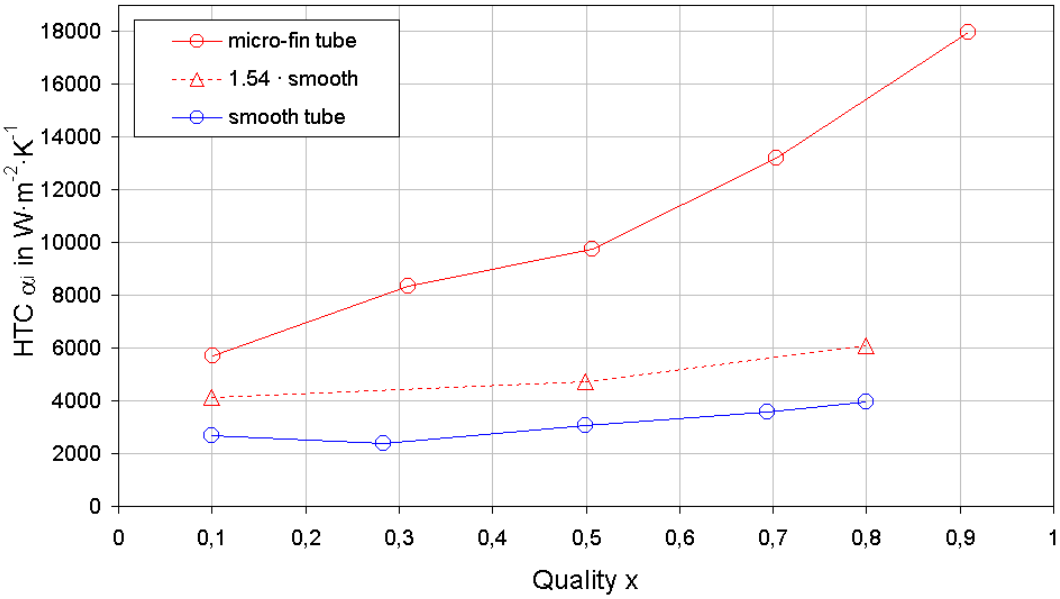

Figure 9.16: Comparison of heat tranfer coefficient of CO_2 inside horizontal smooth and micro-fin tube at varying quality x and t_{sat} = -25 °C and G = 200 kg·m^{-2}·s^{-1}.

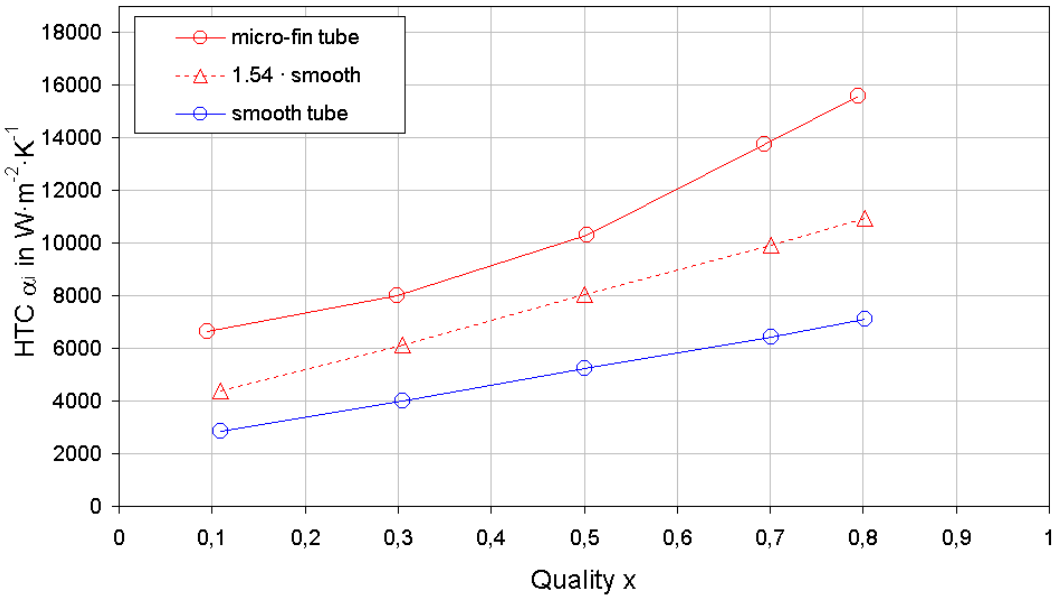

Figure 9.17: Comparison of heat transfer coefficient of CO_2 inside horizontal smooth and micro-fin tube at varying quality x and t_{sat} = -25 °C and G = 400 kg·m^{-2}·s^{-1}.

9.5.2 Comparison of pressure drop

Micro-fin tubes cause higher pressure drop in horizontal and vertical flow than smooth tubes. Figure 9.18 shows a comparison of pressure drop inside horizontal flow for smooth and micro-fin tubes at different mass fluxes. The pressure drop curves of the micro-fin tube are shifted upwards indicating that the micro-fin structure adds a constant pressure drop independent of quality, to the pressure drop of the smooth tube pressure drop. This additional pressure drop is small at low mass flux and highest at highest mass flux. A comparison between pressure drop of the micro-fin and the smooth tube shows that the pressure increase in the micro-fin tube is linear at all mass fluxes.

Since the non linear increase of pressure drop in the horizontal smooth tube was explained by appearing and disappearing of the annular flow regime, it can be assumed that for the micro-fin tube the annular flow regime is present at all mass fluxes.

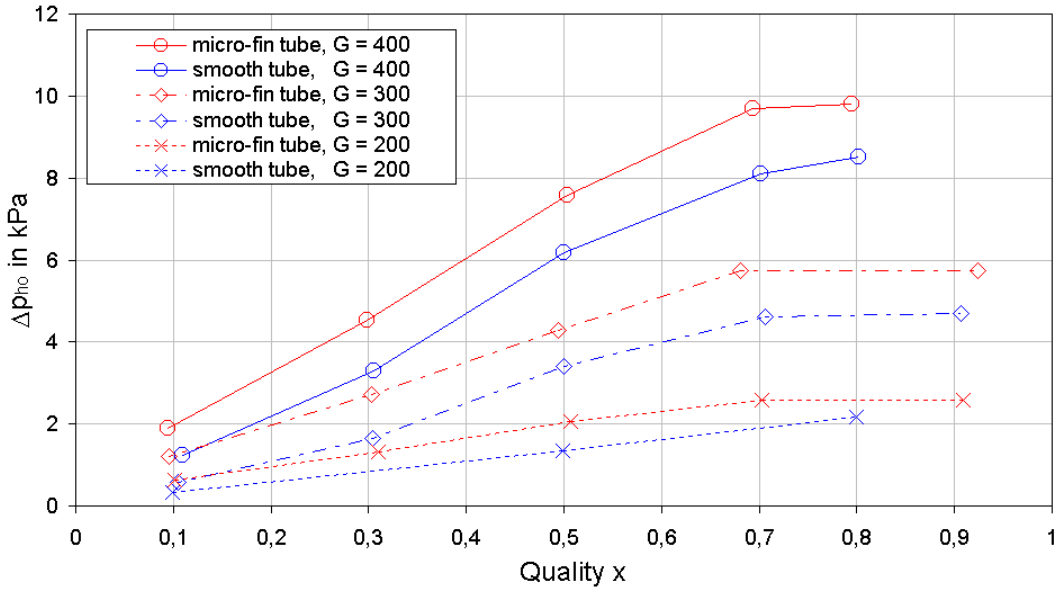

Figure 9.18: Comparison of pressure drop inside horizontal adiabatic smooth and micro- fin tube at varying quality x and t_{sat} = -25 °C. Note that G is in $kg \cdot m^{-2} \cdot s^{-1}$.

Figure 9.19 shows that similar to the pressure drop inside horizontal flow the curves for the micro-fin tube are shifted upwards. A comparison between Figure 9.18 and 9.19, that have identical scales, shows that the increase in pressure drop of micro-fin tube compared to the smooth tube is higher at vertical flow.

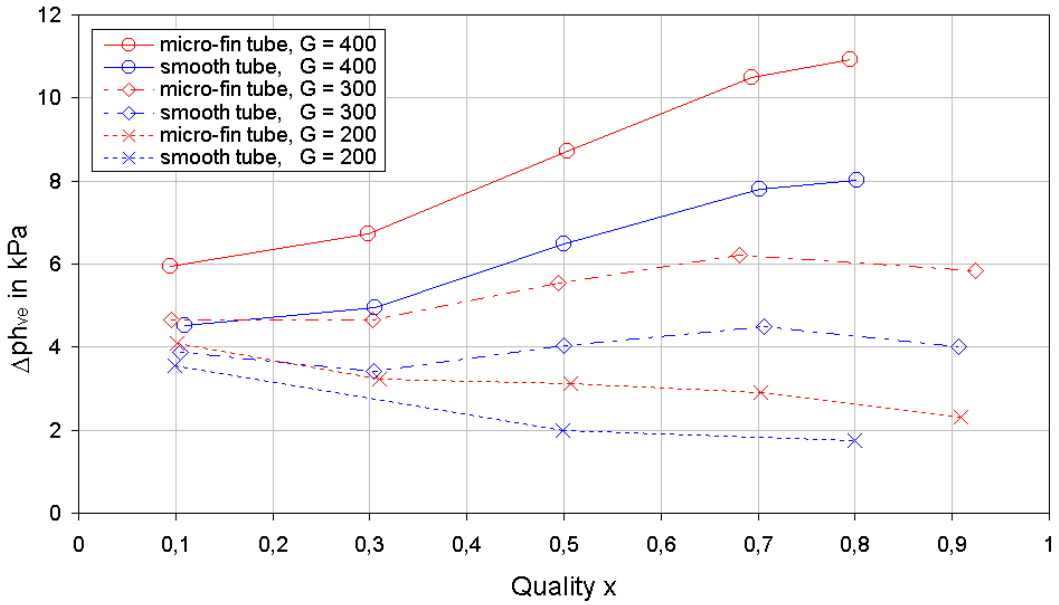

Figure 9.19: Comparison of pressure drop inside horizontal adiabatic smooth and micro-fin tube at varying quality x and t_{sat} = -25 °C. Note that G is in $kg \cdot m^{-2} \cdot s^{-1}$.

9.5.3 Enhancement and penalty factors

Enhancement and penalty factors are defined in Chapter 5.1. Figure 9.20, 9.21 and 9.22 show comparisons of enhancement in HTCs and deterioration in pressure drop for the micro-fin tube at t_{sat} = -15 °C and t_{sat} = -25 °C. According to Figure 9.20 enhancement factors are consistently higher at low mass flux than at high mass flux except for quality x = 0.1. The micro-fin structure may enhance the flow regime better for stratified flow regimes that are present at low mass fluxes. At high mass flux the inner micro-fin surface may be covered by the liquid film of an annular flow regime and thus having less effect on the heat transfer coefficient compared to low mass flux. Enhancement factors are dependent on the saturation temperature at the low mass flux but are much less dependent on saturation temperature at high mass flux.

For the low mass fluxes, enhancement factors increase at higher qualities, whereas enhancement factors at high mass flux are rather independent of qualities. At lower saturation temperature enhancement factors are higher than at higher saturation temperature.

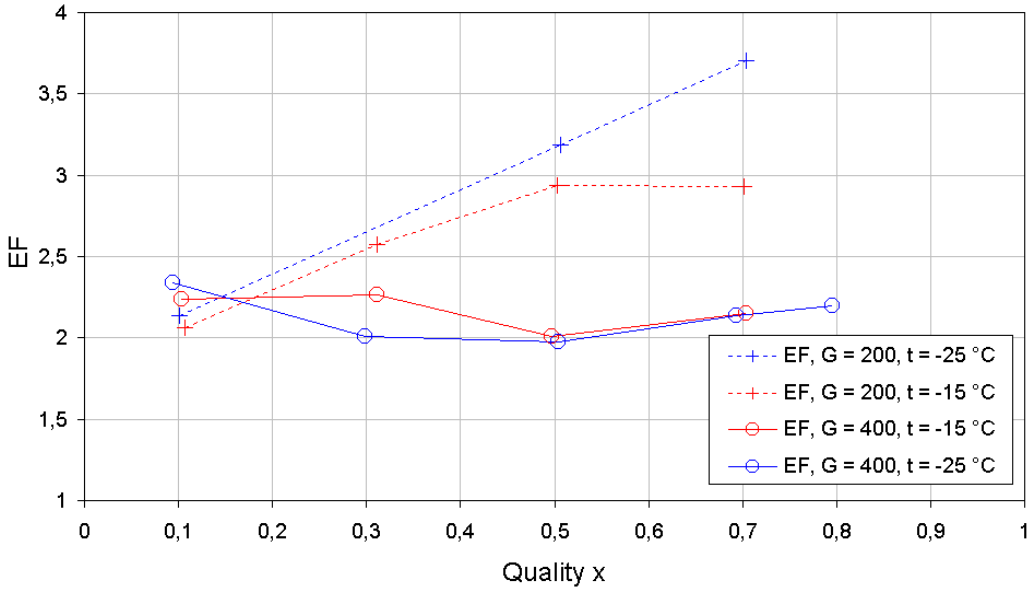

Figure 9.20: Enhancement factors for condensation of CO_2 inside horizontal micro-fin tube at varying quality x, different mass fluxes and saturation temperatures. Note that G is in $kg \cdot m^{-2} \cdot s^{-1}$.

Figure 9.21 shows penalty factors for the micro-fin tube. Penalty factors are highest for low qualities and decrease at higher qualities. For the low mass flux penalty factors are higher than for the high mass flux. The data show that the effect of saturation temperature is not clear for all qualities. One explanation for the decrease of penalty factors with increasing quality may result from the fact that the micro-fin structure increases the frictional pressure gradient at all qualities. The increase in this frictional pressure drop with increasing quality may be less than the increase in pressure drop due to increased flow velocity at higher qualities.

Figure 9.22 shows penalty factors for vertical flow. For high mass flux the penalty factors are not strongly dependent on quality. For low mass flux penalty factors increase with increasing quality.

It can be noted that at all conditions enhancement factors are higher than penalty factors. A direct comparison of enhancement and penalty factors is difficult as the complete refrigeration system has to be taken into

account. Important for an estimation of the improvement of the systems' COP by application of micro-fin tubes is the p-t relationship of the working fluid and the compressors` COP.

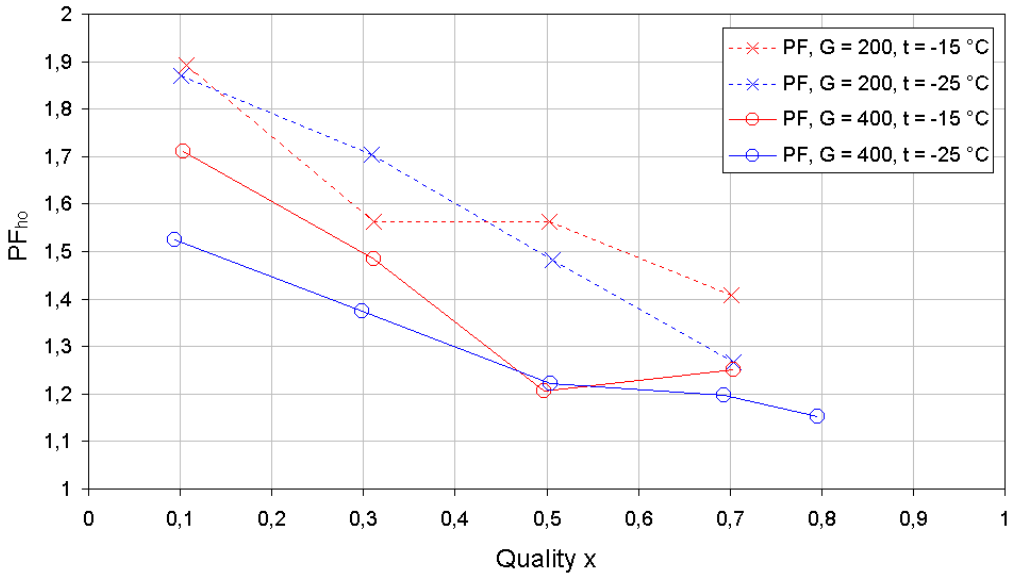

Figure 9.21: Penalty factors for pressure drop inside horizontal tube at varying quality x, different mass fluxes and saturation temperatures. Note that G is in $kg \cdot m^{-2} \cdot s^{-1}$.

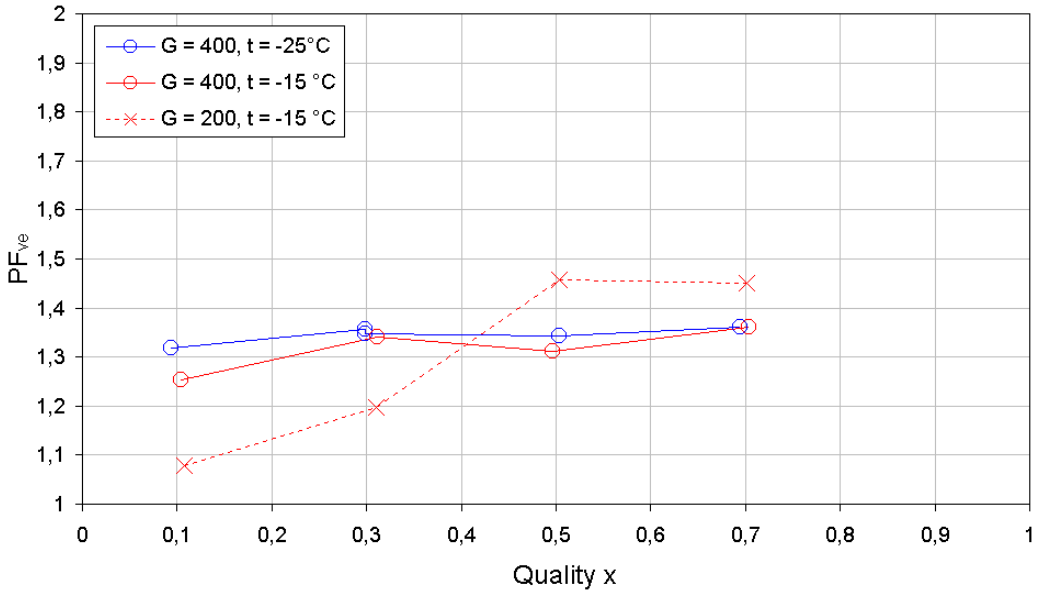

Figure 9.22: Penalty factors for pressure drop inside vertical tube at varying quality x, different mass fluxes and saturation temperatures. Note that G is in $kg \cdot m^{-2} \cdot s^{-1}$.

10. Conclusion

The purpose of this investigation was to present heat transfer coefficient and pressure drop data for condensation of CO_2 inside micro-fin tubes at low temperature. These data was compared to data for heat transfer and pressure drop data from measurements with a smooth tube.

One important result is the fact that heat transfer coefficients of the tested micro-fin tube are independent of the temperature difference between saturation and wall temperature. It was shown that a higher temperature difference gives heat transfer coefficients that are within error bars of heat transfer coefficients at lower temperature differences. This effect is identical for the tested smooth tube.

Data show that for lower saturation temperatures the heat transfer coefficient is significantly higher than for higher saturation temperature. The same effect was shown for the smooth tube.

The increase in heat transfer coefficient of the micro-fin tube compared to the smooth tube is much higher than the increase in heat transfer area of the micro-fin tube. The increase in heat transfer coefficient due to the increase in surface area is only 20% of the total increase at low mass flux. Better distribution of the condensate film and higher turbulence account for this effect.

A comparison of CO_2 data with the predicted heat transfer coefficients by the Cavallini correlation showed that the experimental data for the micro-fin tube are less over predicted than the data for the smooth tube.

Horizontal pressure drop data indicate that annular flow is established at a broader range of quality at the micro-fin tube.

The vertical pressure drop data show interesting behavior at low mass fluxes; the pressure drop actually decreases as quality increases. This information, coupled with the fact that the heat transfer coefficient is insensitive to mass flux, indicate that operating the heat exchanger at low mass fluxes and high qualities would give high heat transfer with reduced pressure loss in vertical sections.

Further experimental data are needed for different micro-fin geometries including different diameters to modify and adjust correlations to predict heat transfer coefficients and pressure drop during condensation of CO_2.

References

[01] F.S. Rowland, M.R. Molina: “Stratospheric sink for chlorofluoromethanes, Chlorine atom catalysed destruction of ozone”, Nature, 249, 174, pp. 810 - 812.

[02] P.B. Whalley: Two-Phase Flow and Heat Transfer, 1996, pp. 5 - 20.

[03] N. Kattan, J.R. Thome, and T. Favrat: Flow Boiling in Horizontal Tubes, Part 1-Development of a Diabatic Two-Phase Flow Pattern Map, 1998.

[04] M.K. Dobson, J.C. Chato, J.P. Wattelet, J.A. Gaibel, M. Ponchner, P.J. Kenney, R.L. Shimon, T.C. Villaneuva, N.L. Rhines, K.A. Sweeney, D.G. Allen, T.T. Hershberger: Heat Transfer and Flow Regimes During Condensation in Horizontal Tubes, Part of ACRC Project 37, May 1994, pp. 19 – 37, 135.

[05] T.A. Shedd: Characteristics of The Liquid Film in Horizontal Two Phase Flow, Ph.D. thesis. UIUC Mechanical Engineering, Illinois, 2001, pp. 100 - 135.

[06] C.Y. Yang, R.L. Webb: “Condensation of R-12 in small hydraulic diameter extruded aluminum tubes with and without micro-fins”. International Journal of Heat and Mass Transfer, 1995, 39(4): pp. 791 - 800.

[07] N. Kattan: Contribution to the Heat Transfer Analysis of Substitute Refrigerants in Evaporator Tubes with Smooth or Enhanced Tube Surfaces, thesis No. 1498, Federal Politechnic School of Lauseanne, 1996, pp. 125.

[08] A. Cavallini, D. Del Col, L. Doretti, G.A. Longo, L. Rosetto: “Heat transfer and pressure drop during condensation of refrigerants inside horizontal enhanced tubes”, International Journal of Refrigeration 23, 2000, pp. 6 - 18.

[09] J. Yu, S. Koyama: “Condensation heat transfer of pure refrigerants in micro-fin tubes", Proc. Int. Ref. Conf at Purdue, 1998, pp. 325 - 30.

[10] A. Cavallini, G.A. Longo, L. Rosetto: “Condensation heat transfer and pressure drop of refrigerants in tubes of finned tube heat exchangers”, Recent Development in Finned Tube Heat Exchangers, Denmark DTI, 1993, pp. 160 - 204.

[11] A. Cavallini, L. Doretti, N Klammsteiner, G.A. Longo, L. Rosetto: “Condensation of New Refrigerants inside Smooth and Enhanced Tubes”, Proc. 19th International congress of refrigeration volume 4, The Hague, 1995, pp. 14 - 105.

[12] A. Cavallini, D. Del Col, L. Doretti, G.A. Longo, L. Rosetto: “Pressure drop during condensation and vaporization of refrigerants inside enhanced tubes”, Heat and technology 15(1), 1997, pp. 3 - 10.

[13] M.A. Kedzierki, J.M. Gonclaves: Horizontal Convective Condensation of Alternative Refrigerants Within a Micro-fin Tube, NISTIR 6095. US Dept. Commerce, 1997.

[14] S. Nonzu, H. Katayama, H. Nakata, H. Honda: “Condensation of refrigerant R-11 in horizontal micro-fin tubes, proposal of a correlation equation for frictional pressure gradient”, Experimental Thermal and Fluid Science, 1998, pp. 18, 82 - 96.

[15] H. Haraguchi, S. Koyama, J. Esaki, T. Fujii: “Condensation heat transfer of refrigerants R-134a, R-123a and R-22 in a horizontal smooth tube and a horizontal micro-fin tube”, 30th National Symposium of Japan, Yokohama, 1993, pp. 5 - 343.

[16] W.F. Stoecker: Design of Thermal Systems, 3rd edition, 1980, pp. 68 - 69.

[17] R.J. Moffat: “Describing the uncertainties in experimental results”, Experimental Thermal and Fluid Science, 1988, Vol 1, pp. 3 - 17.

[18] H. Jaster, P.G. Kosky: “Condensation in a mixed flow regime’, International Journal of Heat and Mass Transfer, 19, 1976, pp. 95 - 99.

[19] J.C. Chato: “Liminar condensation inside horizontal and inclined tubes”, ASHRAE Journal, 4, 1962, pp. 52 - 60.

[20] M.M. Shah: “A general correlation for heat transfer during film condensation inside pipes”, International Journal of Heat and Mass Transfer, 22, 1976, pp. 547 - 556.

[21] A. Cavallini, R. Zecchin: “A dimensionless correlation for heat transfer in forced convective condensation”, Proceedings of the Fifth International Heat Transfer Conference, Japan Society of Mechanical Engineers, 3, 1974, pp. 309 - 313.

[22] D.P. Traviss, W.M. Rohsenhow, A.B. Baron: “Forced convective condensation in tubes, a heat transfer correlation for condenser design”, ASHRAE Transactions, 79(1), 1973, pp. 157 - 165.